Complex subvolcanic magma plumbing system of an alkali basaltic maar-diatreme volcano (Elie Ness, Fife, Scotland)

T. M. Gernon [a,*], B. G. J. Upton [b], R. Ugra [a], C. Yücel [c], R. N. Taylor [a], H. Elliott [a†]

[a] *Ocean and Earth Science, University of Southampton, Southampton SO14 3ZH, U.K.*

[b] *School of GeoSciences, University of Edinburgh, Edinburgh EH9 3JW, UK.*

[c] *Department of Mining Engineering, Gümüşhane University, TR-29000, Gümüşhane, Turkey.*

†*now at: Camborne School of Mines, University of Exeter, Penryn Campus, Cornwall, TR10 9FE, UK.*

Abstract

Alkali basaltic diatremes such as Elie Ness (Fife, Scotland) expose a range of volcanic lithofacies that points to a complex, multi-stage emplacement history. Here, basanites contain phenocrysts including pyrope garnet and sub-calcic augites from depths of ∼60 km. Volcanic rocks from all units, pyroclastic and hypabyssal, are characterised by rare earth element (REE) patterns that show continuous enrichment from heavy REE (HREE) to light REE (LREE), and high Zr/Y that are consistent with retention of garnet in the mantle source during melting of peridotite in a garnet lherzolite facies. Erupted garnets are euhedral and unresorbed, signifying rapid ascent through the lithosphere. The magmas also transported abundant pyroxenitic clasts, cognate with the basanite host, from shallower depths (∼35–40 km). These clasts exhibit wide variation in texture, mode and mineralogy, consistent with growth from a range of compositionally diverse melts. Further, clinopyroxene phenocrysts from both the hypabyssal and pyroclastic units exhibit a very wide compositional range, indicative of polybaric fractionation and magma mixing. This is attributed to stalling of earlier magmas in the lower crust—principally from ∼22–28 km—as indicated by pyroxene thermobarometry. Many clinopyroxenes display chemical zoning profiles, occasionally with mantles and rims of higher magnesium number (Mg#) suggesting the magmas were mobilised by juvenile basanite magma. The tuffs also contain alkali feldspar megacrysts together with Fe-clinopyroxene, zircon and related salic xenoliths, of the 'anorthoclasite suite'—inferred to have crystallised at upper mantle to lower crustal depths from salic magma in advance of the mafic host magmas. Despite evidence for entrainment of heterogeneous crystal mushes, the rapidly ascending melts experienced negligible crustal contamination. The complex association of phenocrysts, megacrysts and autoliths at Elie Ness indicates thorough mixing in a dynamic system immediately prior to explosive diatreme-forming eruptions. *DOI: 10.1016/j.lithos.2016.08.001*

Key words: Alkali basalt, diatreme, clinopyroxene, pyroxenite, magma, eruption

Manuscript accepted for publication in Lithos *15 August 2016*

1 Introduction

Basaltic volcanism takes place in all tectonic settings and accounts for an estimated 80% of all igneous activity at the Earth's surface (Parfitt, 2004). Basaltic magmas are generated as a consequence of partial melting of mantle peridotite (see Hirose and Kushiro, 1993). Such low degree melts then segregate from the refractory residue, and mobilised by thermochemical processes, ascend through the lower lithosphere. Many batches of basaltic melt stall in the 'deep crustal hot zone' (*sensu* Annen et al., 2006), where prolonged interaction with crustal rocks can occur, yet others ascend rapidly from the source experiencing negligible crustal interaction (e.g. Cortés et al., 2015). One possible explanation for this contrasted behaviour is that progressive melt accretion to the conduit walls results in later magmas becoming increasingly shielded from crustal contamination (cf. Tepley et al., 2000).

Maar-diatreme volcanoes—an important class of basaltic landform—are formed as a consequence of rapid magma ascent and explosive eruptions (see Sparks et al., 2006; White and Ross, 2011). Typically these consist of a diverging tephra-filled pipe linking a syn-eruptive crater floor to a hypabyssal 'feeder' system at depth (e.g. Lorenz and Kurszlaukis, 2007; Gernon et al., 2013; Elliott et al., 2015). Ascending basaltic melts are liable to exploit crustal weaknesses, commonly resulting in diatreme localisation along major structural features (e.g. Kurszlaukis and Barnett, 2003; Jelsma et al., 2009; White and Ross, 2011; Son et al., 2012; Brown and Valentine, 2013).

Most maar-diatremes contain lithic fragments ('xenoliths') entrained from the feeder dyke or conduit walls at a range of crustal levels, and occasionally from the upper mantle. Such xenoliths commonly disaggregate during ascent or eruption, liberating crystal fragments or 'xenocrysts' into the host magma. The study of xenoliths, xenocrysts and other crystal fragments from deeply eroded maar-diatremes can yield crucial evidence on the origin, interactions and ascent mechanisms of their parent melts (e.g. Zajacz et al., 2007; Ashchepkov et al., 2011; Yücel et al., 2014).

Geochemical and mineralogical constraints are even more powerful when combined with a physical volcanological understanding of diatreme emplacement, thus yielding insights into the spatio-temporal evolution of the magmas. Here we present data from crystal and lithic inclusions in dykes and pyroclastic deposits of the well-exposed Elie Ness diatreme, SE Scotland (Fig. 1), which records a transition from an initially magmatic eruption style to a dominantly phreatomagmatic mode of eruption (Gernon et al., 2013). We examine and discuss the geochemistry of the different igneous rock units confined to the

* Corresponding author
Email address: Thomas.Gernon@noc.soton.ac.uk (T. M. Gernon).

diatreme, together with the origin and significance of associated (diverse) cognate xenoliths (i.e. autoliths) and lithic inclusions. Our data and observations indicate that the parental magmas originated by low-degree partial melting of a garnet lherzolite source and ascended rapidly, mixing magma batches arrested at various depths, yet experiencing negligible crustal contamination. Our study highlights the complexity of the pre-eruptive magma plumbing system fuelling maar-diatreme volcanism.

2 Geological setting

The Elie Ness diatreme, erupted at ∼290 Ma (Monaghan and Pringle, 2004), is one of >100 diatremes and associated intrusions in Fife and the Lothians, SE Scotland (Fig. 1a–b). These were emplaced during a major phase of Permo-Carboniferous rifting and magmatism across Europe (see Wilson et al., 2004, and references therein). Elie Ness, together with neighbouring diatremes at Elie Harbour, Ardross, Coalyard Hill, Ruddon's Point and Newark, lies along the NE-SW trending Ardross Fault (Fig. 1b)—a right-lateral strike-slip fault, active throughout the late Palaeozoic—inferred to have been exploited by basanitic magmas (Francis and Hopgood, 1970).

The Elie Ness diatreme exposes a stratigraphic thickness of >250 m of tuffs and lapilli tuffs (see Fig. 1c). The deposits are subdivided into three lithofacies associations (LFA, see Gernon et al., 2013). LFA1 is confined to the eastern part of the diatreme (Fig. 1c), and dominantly consists of massive lapilli tuffs, locally containing abundant pyroclastic autoliths and country rock breccias. The tuffs are structureless and poorly to moderately sorted, consisting mainly of juvenile vesicular ash and scoria. Locally, the tuffs comprise sub-vertical lapilli pipes and pod-like accumulations of lapilli. LFA1 is interpreted to represent a pyroclastic deposit formed within the diatreme, mixed with subsided and disrupted pyroclastic material, likely sourced from the overlying (now-eroded) tephra ring (Gernon et al., 2013).

LFA2 dominates most of the pipe-fill at current levels (Fig. 1c), and forms a repetitive succession of massive and well-stratified lapilli tuffs and basalt tuff breccias. The massive lapilli tuffs (on average 0.5–2 m thick) typically infill scour channels developed in underlying strata, and contain abundant angular lithic clasts and blocks. Typically these are overlain by well-bedded (lapilli-) tuffs with diffuse parallel and low-angle cross-stratification, bomb sag structures and rare accretionary lapilli. LFA2 is interpreted to represent a sequence of dilute pyroclastic density current deposits, representing a protracted phase of highly pulsatory phreatomagmatic eruptions, many of which were potentially sourced from a neighbouring vent to the east (Gernon et al., 2013).

LFA3 comprises a series of minor discordant intrusions, including a 500 m wide basanitic breccia pipe to the west (Fig. 1c), and a number of volcaniclastic and magmatic dykes of basaltic and trachybasaltic composition. The breccia pipes are thought to relate to debris-jet emplacement, linked to a feeder dyke that interacted with groundwater at some level within the diatreme. The dykes signify an episode of passive magma intrusion during the waning phase of volcanism at Elie Ness (Gernon et al., 2013).

3 Analytical methods

The Elie Ness diatreme was mapped at a scale of 1:2,270 (Fig. 1c). The lithofacies were recorded on graphic logs of a cumulative total of ∼250 m strata, enabling correlation of beds based on grain-size, texture, composition and sedimentary structures (Gernon et al., 2013). Representative samples were collected from regular intervals across the diatreme (Fig. 1c), capturing the different lithofacies and intrusives bodies. A total of twenty polished thin sections were analysed using optical and scanning electron microscopy (SEM: Leo 1450 VP, operated at 25 keV using energy-dispersive X-ray spectroscopy (EDS)).

Whole-rock major elements were analysed using X-ray fluorescence (XRF) (Panalytical Magix-Pro WD-XRF fitted with a 4kW Rh X-ray tube) at the University of Southampton. Calibration was via 20+ international geochemical reference samples. Solution inductively coupled plasma mass spectrometry (ICP-MS) was performed to determine the concentration of incompatible elements using a ThermoScientific XSeries2 at the University of Southampton; samples were prepared following the standard procedure of silicate rock dissolution by HF digest (adapted from Beauchemin, 2008).

Major element analysis of zoned and unzoned pyroxene crystals from selected samples (5, 10, 14 & 17) was carried out using a Cameca SX-100 electron probe micro-analyser (EPMA) in the School of Earth Sciences at the University of Bristol. Analyses were performed using operating conditions of 15 kV and 80 nA and a focused spot size of 1 μm. Earlier analyses by B.G.J.U. on sample 1L were performed at the Department of Geology and Geophysics, University of Edinburgh, on a Cambridge Scientific Instruments Microscan 5 electron-probe micro-analyser using the wavelength dispersive method. Pure elements, oxides and simple silicate compositions were used as standards. The operating conditions were 200 kV, using a sample current of 30 nA.

4 Results | Erupted rocks of the Elie Ness diatreme

4.1 Alkali basalts, trachybasalts and basanites

The rocks investigated in this study are classified as basalts, trachybasalts and basanites (Fig. 2a; see Table 1). Together with a suite of similar, albeit older (i.e. Lower Carboniferous) volcanics in Scotland (Smedley, 1988), the rocks are classified as alkaline basalts (Fig. 2b) on the basis of their Nb/Y versus Zr/TiO_2 compositions (sensu Winchester and Floyd, 1977), and as within-plate alkali basalts based on Nb-Zr-Y (Meschede, 1986). Whole-rock analyses of representative tuffs and minor intrusives at Elie Ness show a limited compositional range with MgO between 8.7 and 10.8 wt.% (Table 1; see also Table 5.1 in Wallis, 1989). Indeed, the total alkali and silica contents are broadly comparable to other Permo-Carboniferous volcanics in Scotland (Fig. 2a), which include the Passage Group lavas, Ayrshire sills, Mauchline group, Fife and Lothian sills and basanite lavas, and the Highland dykes (Wallis, 1989).

All LFA samples have $Zr/Nb \leq 5$ (Fig. 3a; Tables 1–2), and Zr/Y–Nb/Y that place the samples above the MORB field in the mantle plume array (Fig. 3b). The Nb-Zr-Y contents (Figs. 2a–3) are again comparable to those of the aforementioned Permo-Carboniferous volcanics described by Wallis (1989). The chondrite-normalised rare earth element (REE) patterns for all samples are characterised by a progressive enrichment from Lu through to La (Figs. 4a–c) with La_n/Yb_n typically in the range 14–27. Abundances of La are around 80–200 times chondrite. Primitive mantle-normalised trace elements (Figs. 4d–f) also reflect an enrichment towards the more incompatible elements. This is particularly apparent in the progressively higher normalised abundances between Y and Nb. Sr is an exception in that it generates a dip relative to Ce–Nd in LFA1 and LFA2 (Figs. 4d–e).

The strongly negative Ba anomaly observed in one sample (S4, Fig. 4d) is most readily explained by Ba mobility during basalt alteration; indeed this sample shows evidence of sericitic alteration, which is a potential sink for Ba and may lead to erratic barium abundances (Du Bray et al., 1995). Similarly, the fact that Pb concentrations are scattered, yet are dispersed around the Ce_n and Nd_n values (Figs. 4d–f), is consistent with hydrothermal alteration. For example, the porous breccia pipe (S10)—more susceptible to fluid flow—exhibits a positive Pb anomaly, whereas the coherent dyke (S17) lies directly between Ce_n and Nd_n (Fig. 4f) presumably as it was less accessible to hydrothermal fluids.

4.2 Xenoliths and crystals / observations and review

The basalts, trachybasalts and basanites—pyroclastics and intrusives—contain abundant xenoliths and crystals (xenocrysts and phenocrysts), akin to many Permo-Carboniferous volcanics in Scotland (e.g. Chapman, 1976; Upton et al., 1998, 2003, 2009). The diatreme contains two categories of highly contrasted cognate materials: (a) pyrope garnets (colloquially referred to as 'Elie rubies') and sub-calcic augites that are likely representative of a high-pressure (∼2 GPa) phenocyst assemblage, and (b) a suite of pyroxenite and related autoliths, together with alkali feldspar megacrysts and co-magmatic felsic rocks. This second category is thought to represent products that crystallised in the vicinity of the crust-mantle discontinuity at ∼35–40 km depth (Bamford et al., 1978; Upton et al., 1983). In the intrusive bodies (LFA3, Fig. 1c), accidental xenoliths are rare and generally restricted to metagabbro and quartz-feldspathic gneiss probably of lower to mid-crustal derivation.

In this section, we summarise the pertinent characteristics of xenolith and crystal assemblages recorded at Elie Ness, combining empirical observations of these fragments in thin section, and drawing extensively on published accounts, including exhaustive studies by Chapman (1976) and Upton et al. (2003).

4.2.1 Garnet crystals and their significance

The pyrope garnet crystals are typically <1 mm but up to ∼50 mm in diameter (Fig. 5a), commonly exhibiting euhedral form (i.e. rhombic dodecahedron with bevelled edges, occasionally with faces of the octahedron; see Upton et al., 2003). The garnets are titaniferous (∼0.4 wt.% TiO_2) and have low Cr_2O_3 contents (0.01–0.19 wt.%) (Chapman, 1976; Upton et al., 2003). Sub-calcic augites also occur, and their compositional similarity to those co-crystallised with titanian pyrope in the Kakanui diatreme (New Zealand; Dickey, 1968) suggest that these might similarly have been in equilibrium with garnet. The pressure at which the pyrope and sub-calcic augite were in equilibrium with melt is inferred to have been approximately 2 GPa (Colvine, 1968; Chapman, 1974a, 1976; Upton et al., 2003).

4.2.2 Pyroxenite xenoliths: a synthesis

Lustrous black ultramafic xenoliths, with diameters up to ∼50 mm occur in the tuffs and intrusions (Fig. 5b-c), and are interpreted as cognate cumulates (see Chapman, 1976). Most are hornblende pyroxenites, composed largely of salitic augite and pseudomorphs after olivine (carbonated or serpentinised), enveloped by kaersutite oikocrysts up to 10 mm across. Minor accessories

include biotite, apatite and opaque oxides. The pyroxenites display a wide variety of textures and modes, ranging from olivine-kaersutite clinopyroxenites through olivine-free hornblende pyroxenites via hornblende pyroxenites with late sodic feldspar to amphibole-free varieties with biotite and/or sodic plagioclase. On textural and mineralogical criteria, the cumulate nodules have been subdivided into five types, collectively thought to represent a differentiation series (refer to Chapman, 1974a, 1976).

Olivine and clinopyroxene are inferred to represent cumulus phases, whilst kaersutitic amphibole, biotite and sodic feldspar were intercumulus. The kaersutite oikocrysts (Fig. 6a) constitute up to 40 modal%. Chlorite in some pyroxenites (Fig. 6b) is presumed to be pseudomorphous after intercumulus glass, and—if so—indicates that these pyroxenites were still above their solidus at the time of entrainment. Calcitic ocelli, typically chlorite-rimmed (Fig. 6c), also occur in both late-stage amphiboles and the inferred glassy residues (Fig. 6b).

With loss of olivine and then pyroxene, this suite of xenoliths is inferred to grade into less frequent biotite-rich ultramafic xenoliths (Fig. 6d). Olivine pyroxenites and clinopyroxenites lacking hydrous phases also occur, but again are rare. Some pyroxenites contain pseudomorphs after idiomorphic olivine enclosed in well-equilibrated mosaics of equigranular augite and hornblende showing 120° triple junctions. In other pyroxenites, larger augite crystals are surrounded by smaller pyroxene neoblasts (Fig. 6e), whilst elsewhere the pyroxenes have been partially replaced by secondary amphibole along cleavage planes and grain boundaries (Chapman, 1976). The hornblendites in some of the basanites may have grown as metasomatised pyroxenites in which the pyroxenes were wholly replaced by kaersutite. Some pyroxenes and olivines are idiomorphic and occasionally euhedral. Pyroxenes in the Elie Ness autoliths commonly show oscillatory zonation and some exhibit hourglass zoning (Fig. 6f).

4.2.3 Anorthoclasite xenoliths and zircon

Feldspars (anorthoclase, K-albite and sanidine) occur as discrete crystals, and as xenoliths dominated by Na-rich feldspar. Anorthoclase megacrysts, up to several cm across, occur in the tuffs and minor intrusives. Scarce zircon megacrysts (>10 mm diameter) are regarded as co-magmatic with the anorthoclasite/albitite xenoliths (see Irving and Frey, 1984; Hinton and Upton, 1991). Oscillatory zoning in the zircons corresponds to abrupt changes in REE, Th and U contents, suggesting dynamic growth conditions in these melts, as recorded in other Scottish megacrysts (Hinton and Upton, 1991; Upton et al., 1999). Similar zircons in the neighbouring Coalyard Hill vent exhibit quasi-euhedral morphologies, and their association with 'anorthoclasite'

xenoliths suggest they grew in a felsic magma, which subsequently mixed with the basanite (Chapman and Powell, 1976). The Elie Ness tuffs also contain (rare) coarse-grained polycrystalline anorthoclasite and albitite clasts composed mainly of sodic feldspar, comparable to those in other diatremes along the Ardross Fault.

4.2.4 Alkali feldspar megacrysts: observations and review

Alkali feldspar cleavage fragments are presumed to be derivative from coarse anorthoclasite rocks comparable to those found as xenoliths (Aspen et al., 1990; Upton et al., 2009). Electron microprobe analysis of the feldspars yield a composition of $\sim An_{1.8}Ab_{80.1}Or_{17.7}Cn_{0.1}$; however, these megacrysts span the broadest compositional range yet seen in any of the Scottish localities, ranging from K-albite via sodic anorthoclase, to nearly pure sanidine (i.e. $Or_{7.5}$–Or_{99}). Commonly there is a patchy replacement of 'primary' anorthoclase by more potassic feldspar, and late high-K feldspar veinlets. These bilaterally symmetrical veinlets (nearly pure $KAlSi_3O_8$) are similar to those described from an anorthoclasite xenolith in the Southern Uplands (Upton et al., 1999, 2011). Most of the discrete feldspar crystals are likely to represent cleavage fragments from (pegmatitic) anorthoclasite veins or dykes, although through analogy with the neighbouring Coalyard Hill diatreme, some might represent high-pressure phenocrysts in evolved melts that were intercepted by the basanitic host magmas (Chapman and Powell, 1976; Aspen et al., 1990; Upton et al., 2011).

5 Clinopyroxene and alkali feldspar analysis

Clinopyroxenes and some alkali feldspars from the tuffs, breccias and dykes (Fig. 1c) were analysed by electron-microprobe (see methods). Whilst some pyroxenes retain idiomorphic form, the majority of the pyroxene crystals (and alkali feldspars) were cleavage fragments. According to the International Mineralogical Association (Morimoto et al., 1988) the pyroxenes (Table 3) are subdivided mainly as diopsides and augites (Fig. 7), with magnesium numbers (Mg# = Mg/(Mg + Fe_{tot})) ranging from 0.49 to 0.84. Some clinopyroxenes have high Wo contents (>Wo_{50}), and a few extreme compositions with high Fe/Mg and Na_2O are hedenbergite (Fig. 7).

Zoned clinopyroxenes are abundant in LFA3, and of comparatively low abundance in both pyroclastic lithofacies associations (LFAs 1–2), where they are more fragmented. In many cases, the clinopyroxenes are strongly zoned (see Table 3; Fig. 8; Supplementary Fig. 1), with discrete crystals showing normal and reverse zonation. Although numerous crystals exhibit cores with more

primitive compositions (i.e. relatively high Mg# and Cr_2O_3, e.g. S10-34, Table 3; Supplementary Fig. 2), in some cases the mantles and rims of the clinopyroxenes exhibit higher Mg# (dark areas in the BSE images) relative to their cores (e.g. S17-40, Fig. 8, and S10-71, S10-73 & S17-81, see Supplementary Fig. 2).

The wide range of clinopyroxene compositions is shown in plots of CaO vs. Al_2O_3 and Na_2O vs. Al_2O_3 (Figs. 9a,d) with CaO ranging from ∼16 to >24 wt.%, Al_2O_3 from ∼1 to >15 wt.% and Na_2O from ∼0.5–3.4 wt.%. Wide scatter is seen in plots of TiO_2 vs. Al_2O_3 and Al_2O_3 vs. SiO_2 (Figs. 9b,c) with crude positive and negative correlations respectively (TiO_2 contents vary from ∼0.1–>4 wt.%). A closer (negative) correlation is shown for MgO vs. FeO (Fig. 9e) with MgO ranging from ∼7–17 wt.% and total iron (as FeO) from ∼3–17 wt.%. The few clinopyroxenes exhibiting comparatively high Fe/Mg and Na contents are comparable to those of megacrysts and anorthoclasites described from other Scottish localities (refer to p. 948 of Upton et al., 2009). Indeed, they are also compositionally similar to clinopyroxene megacrysts and xenoliths from Highland intrusions of comparable age (i.e. Colonsay, Stob a' Ghrianain and Streap Comlaidh, see Wallis, 1989).

The clinopyroxenes are subdivided further using Mg# vs. Cr_2O_3 (Fig. 10a), Mg# vs. TiO_2 (Fig. 10b), and Ti (apfu) vs. Al (apfu) (Fig. 10c). High Cr_2O_3 and Mg# reflect more primitive compositions (Fig. 10a), and it can be seen that the majority of these correspond to crystal cores (Fig. 10d). They display negative trends in Mg# vs. TiO_2 but positive trends in Al_{tot} vs. Ti (apfu) (Fig. 10 b–c) from the most primitive to the most evolved compositions (cf. Jankovics et al., 2012).

In general, the rims to zoned clinopyroxene have comparably low Cr_2O_3 (typically <0.1 wt.%, Fig. 10d), high Mg# (typically of the order 0.7–0.8; Fig. 10d–e), high TiO_2 (typically >2 wt.%, Fig. 10e), and high Al_2O_3 (Table 3), with Ti:Al values typically in the range 0.25–0.4. In contrast, the majority of cores generally exhibit higher Cr_2O_3 (∼50% >0.1 wt.%), lower TiO_2 (most ≤2 wt.%), moderate to high Mg# (Fig. 10d–e; Supplementary Fig. 2) and Ti:Al values mostly of the order 0.125–0.25 (Fig. 10f). Some crystals exhibit ragged cores (e.g. S10-57), whereas other cores resemble euhedral phenocrysts (S17-12, Fig. 10e).

Finally, the feldspar cleavage fragments have compositions ranging from albite and anorthoclases to sanidines (Na_2O: ∼0–11.5 wt.%: K_2O: ∼1–∼17 wt.%; Fig. 9f).

5.1 Pyroxene thermobarometry

The temperature and pressure, and hence crystallisation depth of volcanic rocks can be estimated using clinopyroxene compositions (Nimis, 1995; Nimis and Ulmer, 1998; Nimis and Taylor, 2000) and clinopyroxene–liquid equilibria (Putirka et al., 1996, 2003). More quantitative P-T estimates using clinopyroxene composition have been re-evaluated by Putirka (2008); by using Fe–Mg exchange and $K_D(\text{Fe–Mg})_{cpx-liq}$, this yielded an equilibrium constant = 0.27 ± 0.03.

Quantitative pressure and temperature estimates for the Elie Ness pyroxenes were obtained using the clinopyroxene-only and clinopyroxene-liquid barometric and thermometric equations of Putirka (2008). The parent liquid compositions were approximated using whole-rock (XRF) compositions. The equilibrium constants were calculated for clinopyroxene compositions from the basanitic breccia pipe (sample 10) and trachybasaltic dyke (sample 17): two clinopyroxene compositions were identified as being in equilibrium with the melt, according to the Putirka equilibrium constant (0.27 ± 0.3) (Table 4). In contrast, clinopyroxene crystals from the tuffs were found not to be in equilibrium with the melt; this is perhaps not surprising given that the tuffs comprise a complex mixture of pyroclastic and magmatic deposits from a variety of sources (e.g. mass wasting of crater walls; Gernon et al., 2013). The calculated results of clinopyroxenes from the breccia pipe (Table 4) reveal high mean pressures of 0.7 ± 0.16 GPa and temperatures of 1166 ± 43 °C. The P and T estimates for the dyke are within error of this at 0.9 ± 0.27 GPa and 1188 ± 72 °C (Table 4), corresponding to approximate crystallisation depths of 22–28 km.

6 Discussion | Complexity of the magma 'supply chain'

6.1 Petrogenesis

The Elie Ness parental magmas are assumed to have an asthenospheric origin (>70 km Wallis, 1989). The high MgO contents (> 8 wt.%) of all sampled basaltic hosts (Table 1; see Wallis, 1989) indicate that they represent relatively primitive magmas that have not experienced significant fractionation and are close to parental melt compositions. High Zr/Y and Nb/Y (Fig. 3), alongside the generally high incompatible element contents, provide evidence for small degrees of partial melting (<5%). The REE patterns, progressively enriched from Lu to La, and the high Zr/Y are consistent with retention of garnet in the mantle source. As garnet is considered to be a phenocryst phase in Elie Ness,

it is inferred that the HREE were retained either during garnet crystallisation and accumulation during magma ascent, or were held in garnet during melting of peridotite in a garnet lherzolite facies.

Negative Sr in the trace element patterns (Figs. 4d–f) is extremely unlikely to relate to plagioclase fractionation, given the absence of feldspar as a crystallising phase in the basanitic magmas (with their low Ca/Al ratios), and the absence of a negative Eu anomaly (Fig. 4a–c). Hence the Sr concentration may be a feature of the mantle source (akin to kimberlites; e.g. Le Roex et al., 2003) or crustal contamination (e.g. Elburg and Soesoo, 1999). Given the primitive nature of the samples and the lack of any other indications of crustal contamination such as Th/La $\gtrsim 0.15$, coupled with relatively low $^{87}Sr/^{86}Sr$ ratios (0.7032–0.7049) and high $^{143}Nd/^{144}Nd$ ratios (0.5122–0.5126) (see Wallis, 1989), the low Sr is most likely a mantle characteristic. Pb concentrations are not systematically enriched relative to equivalently incompatible REE (Fig. 4), indicating a negligible role for crustal contamination.

The pyrope garnets and low-Ca augites are inferred to represent high-pressure phenocrysts that crystallised from basaltic melts deep in the lithospheric mantle (∼50–60 km; Fig. 11) (Colvine, 1968; Chapman, 1976; Upton et al., 2003). The survival of garnet (Donaldson, 1984) points to very rapid ascent rates, which for alkali basaltic magmas containing peridotite xenoliths, is estimated to be of the order of 10 ms^{-1} (Kuo and Kirkpatrick, 1985)—broadly comparable to rates obtained from studies of garnet dissolution in kimberlites (Canil and Fedortchouk, 1999). Rapid ascent of such crystal-laden magmas invokes the presence of an exsolved fluid phase, perhaps linked to decompression-induced CO_2 exsolution during magma ascent (cf. Stoppa, 1996; Stoppa et al., 2003; Mattsson and Tripoli, 2011).

6.2 Clinopyroxene variability

The very broad compositional range exhibited by clinopyroxenes (Figs. 9a–e & 10) indicates a wide range of pressures, temperatures and magma compositions, and in summary, can be considered in three categories:

(1) Crystals derived from fragmentation of pyroxenitic cumulates. From the petrographic indications that some pyroxenites were above their solidus temperatures at the time of entrainment, they are assumed to be cognate to the host magma (cf. Chapman, 1976). The comparative abundance of pyroxenite autoliths at different stratigraphic levels in the tuffs implies energetic pulses of magma through the protolith sequence.
(2) Discrete Na-rich pyroxene crystals (Fig. 9d), known from other Scottish xenolith/megacryst suites, compositionally resemble those found in

anorthoclase-pyroxene-magnetite-apatite associations. Accordingly these are regarded as part of the 'anorthoclasite suite' (*sensu* Upton et al., 1999).

(3) Phenocrysts crystallised under a variety of conditions ranging from deep lithospheric to near surface. Pyroxene thermobarometry suggests that crystallisation of a subset of these pyroxenes (i.e. late effusive eruptive phase of LFA3) commenced in lower-crustal magma reservoirs at ∼22–28 km, broadly equivalent to the depth of mafic reservoirs in modern-day rift settings (e.g. Ronga et al., 2009).

The clinopyroxene crystal fragments exhibit a very wide compositional range in both the intrusive and extrusive rocks (Fig. 9a–e), pointing to extremely thorough mixing of magma batches from various depths, probably within a lower-crustal reservoir prior to eruption (cf. Montagna et al., 2015). Fractional crystallisation of magmas is indicated by the Fe/Mg variation (Fig. 9e), whilst the variation in Ca-Tschermak's molecule, suggested by the variance in SiO_2, CaO and Al_2O_3 (Figs. 9a–c), points to a polybaric evolution. This can be explained by the presence of a stock-work of semi-independent magma reservoirs beneath the diatreme (cf. Yücel et al., 2014), which were disturbed and entrained by the rapidly ascending basanite magma.

Elsewhere, high Mg and Cr clinopyroxenes have been interpreted as xenocrysts that formed in the mantle or deep crust (e.g. Barton and van Bergen, 1981; Zhu and Ogasawara, 2004; Akinin et al., 2005; Zhang et al., 2007), or as reflecting high-pressure fractionation and mixing processes during the same magmatic episode (e.g. Wass, 1979; Duda and Schmincke, 1985; Fodor et al., 1995). Compositional changes observed within individual clinopyroxene crystals (Figs. 8, 10d–f, Supplementary Figs. 1–2) can be interpreted as step zoning and show multiple growth events in some cases from more mafic magmas (e.g. Duda and Schmincke, 1985; Streck et al., 2007; Streck, 2008), probably indicting periodic replenishment of the shallower magma reservoir by primitive basaltic melts (cf. Streck et al., 2002). However, several clinopyroxene crystals show complex oscillatory zoning and many also record a shift from primitive to more evolved melts (see Figs. 10d–f & Supplementary Figs. 1–2). Further, the presence of both normally and reversely zoned clinopyroxenes within the same rock sample is consistent with magma mixing and/or an increase in temperature and Mg/Fe^{2+} ratio (Anderson, 1974; Pe-Piper, 1984).

6.3 Regional variability in diatreme composition

It is noteworthy that the nearby basanitic Elie Harbour diatreme (see Fig. 1b) did not erupt any xenoliths, autoliths or high-pressure phenocrysts. Further, the absence of upper mantle lherzolite xenoliths at Elie Ness is enigmatic since

these are present in several neighbouring basanitic diatremes that also contain analogous pyroxenitic xenoliths and anorthoclasite debris (e.g. Coalyard Hill; Chapman, 1974b, and Ruddon's Point). One possible explanation is that the Elie Ness magmas crystallising garnet and sub-calcic augite did not have the erosive capability to entrain pieces of their sidewalls, but were sufficiently energised at near-Moho levels (possibly due to copious CO_2 exsolution) to disaggregate and transport pyroxenite and 'anorthoclasite suite' fragments to surface levels.

Significant mineralogical differences within the East Fife cluster may suggest that eruptions sampled the deep lithosphere on length-scales of individual diatremes, as documented in monogenetic volcanoes in modern rift systems, where the distribution of melt is similarly controlled by large-scale lithospheric structures (Rooney et al., 2011). Speculatively, movement along major structures such as the Ardross Fault might have provided a pathway for magmas to traverse the lithospheric mantle, without tearing peridotite from the conduit margins. Nonetheless, evidence for negligible crustal contamination is most readily explained by rapidly ascending magmas exploiting the same pathway—at least from mid to upper crustal levels—with accreted material insulating magmas from crustal contamination (cf. Tepley et al., 2000).

6.4 Implication for physical volcanological emplacement

Our data and petrological constraints provide a 'cradle-to-grave' insight into the deep and shallow magma plumbing systems fuelling alkali basaltic maar-diatreme eruptions. Accordingly, the three lithofacies associations (Fig. 1c) capture different stages in the life-cycle of a maar-diatreme volcano (Fig. 12). For instance, LFA1 constitutes vent-filling massive lapilli tuffs, inferred to represent an early eruptive phase driven primarily by magmatic volatiles (Gernon et al., 2013). Given that LFA1 represents progressive infilling and mixing of the diatreme through repetitive eruptive bursts and subsidence of pyroclastic material (cf. Gernon et al., 2009), it is not surprising that these samples show significant variation in chondrite-normalised REE patterns (Figs. 4a–c) and primitive mantle-normalised trace element patterns (Figs. 4d–f).

In contrast, LFA2 (overlying LFA1) shows very little variation in REE and trace element patterns (Fig. 4), which is surprising, given the samples were collected through a sequence of >50 bedded tuffs and lapilli tuffs (Fig. 1c) with a cumulative thickness of >65 m (Gernon et al., 2013). The assemblage of structures and nature of pyroclasts (Gernon et al., 2013) are consistent with small pulsatory phreatomagmatic eruptions (see Lorenz, 1986; White and Ross, 2011), resulting from high-level interactions between ascending magmas and external water. However, volcanism was necessarily driven by magmatic

volatiles (see Sparks et al., 2006) to explain the preservation of unstable mineral phases. Geochemical similarities between a neighbouring vent to the east (S8, Fig. 1c) and the majority of tuff packages from LFA2, supports the hypothesis that many flows were derived from an external source ∼200 m to the east (Gernon et al., 2013).

The late-stage coherent trachybasaltic and basanitic dykes of LFA3 (Fig. 1c) exhibit the most considerable variability in REE and trace element concentrations (Tables 1–2, Fig. 4). These relatively shallow magmas (i.e. ∼22–28 km), containing abundant zoned clinopyroxenes (e.g. Fig. 8), were likely destabilised by deep-sourced basanite magma involved in the eruption of LFAs 1–2 (Fig. 12). Given the abundance of mafic phases including clinopyroxene and amphibole in the LFA3 intrusives, the observed chemical heterogeneity is very likely due to the accumulation of entrained mafic phases—a process invoked to explain similar patterns in Spanish lamprophyres (Ubide et al., 2014). The shift towards effusive activity recorded by LFA3 reflects a lesser role for phreatomagmatism during the waning stages of eruption (Gernon et al., 2013).

7 Concluding remarks

Elie Ness is remarkable for the complex assemblage of lithic inclusions, crystals—and inferentially former melts—signifying a wide range of pressures, temperatures and melt compositions. For all of these components to have been evacuated in the explosive tuff-forming eruptions requires a culminating flux of basanite magma through the subvolcanic plumbing system, that evacuated magmas in differing stages of evolution. We propose that energetic magma flows transport the deep crystals, disaggregate and entrain earlier-formed 'anorthoclasite suite' xenoliths approximately at Moho levels (produced from several previous replenishments of 'underplated' chambers, Fig. 11), and then flush out minor pockets in which preexisting magma batches had been equilibrating at lower pressures (i.e. depths of ∼22–28 km; Fig. 11). Based on the euhedral, unresorbed form of garnets—combined with the preservation state of alkali feldspars and 'anorthoclasite suite' inclusions—transport from the lithospheric mantle to the surface was necessarily very rapid (order of hours to days) (cf. Canil and Fedortchouk, 1999). An initially explosive phase driven by magmatic volatiles, involving diatreme excavation and pyroclastic infill processes, was followed by pulsatory phreatomagmatic eruptions and a final effusive stage (Fig. 12), with remarkably little bulk geochemical variation occurring throughout the eruptive life-cycle.

Acknowledgements

Gernon was supported by the Clough and Mykura Fund of the Geological Society of Edinburgh, and the Timothy Jefferson Fund of the Geological Society of London. We thank Stuart Kearns and Matthew Cooper for their assistance with the EPMA and XRF respectively. Figure 12 was illustrated by Gary Hincks. We thank Andrew Kerr for his editorial assistance, and Aniko Batki and Teresa Ubide for very helpful comments that greatly improved the manuscript.

References

Akinin, V. V., Sobolev, A. V., Ntaflos, T., Richter, W., 2005. Clinopyroxene megacrysts from Enmelen melanephelinitic volcanoes (Chukchi Peninsula, Russia): application to composition and evolution of mantle melts. Contributions to Mineralogy and Petrology 150 (1), 85–101.

Anderson, A. T., 1974. Evidence for a picritic, volatile-rich magma beneath Mt. Shasta, California. Journal of Petrology 15 (2), 243–267.

Annen, C., Blundy, J. D., Sparks, R. S. J., 2006. The genesis of intermediate and silicic magmas in deep crustal hot zones. Journal of Petrology 47 (3), 505–539.

Ashchepkov, I. V., André, L., Downes, H., Belyatsky, B. A., 2011. Pyroxenites and megacrysts from Vitim picrite-basalts (Russia): Polybaric fractionation of rising melts in the mantle? Journal of Asian Earth Sciences 42 (1–2), 14–37.

Aspen, P., Upton, B. G., Dickin, A. P., 1990. Anorthoclase, sanidine and associated megacrysts in Scottish alkali basalts: high-pressure syenitic debris from upper mantle sources? European Journal of Mineralogy 2 (4), 503–518.

Bamford, D., Nunn, K., Prodehl, C., Jacob, B., 1978. LISPB —IV. Crustal structure of Northern Britain. Geophysical Journal International 54 (1), 43–60.

Barton, M., van Bergen, M. J., 1981. Green clinopyroxenes and associated phases in a potassium-rich lava from the Leucite Hills, Wyoming. Contributions to Mineralogy and Petrology 77 (2), 101–114.

Beauchemin, D., 2008. Inductively coupled plasma mass spectrometry. Analytical Chemistry 80, 4455–4486.

Brown, R. J., Valentine, G. A., 2013. Physical characteristics of kimberlite and basaltic intraplate volcanism and implications of a biased kimberlite record. Geological Society of America Bulletin 125 (7-8), 1224.

Canil, D., Fedortchouk, Y., 1999. Garnet dissolution and the emplacement of kimberlites. Earth and Planetary Science Letters 167 (3-4), 227–237.

Chapman, N. A., 1974a. Petrology of inclusions from some late Palaeozoic British volcanic rocks. Ph.D. thesis, University of Edinburgh.

Chapman, N. A., 1974b. Ultrabasic inclusions from the Coalyard Hill Vent, Fife. Scottish Journal of Geology 10 (3), 223–227.

Chapman, N. A., 1976. Inclusions and megacrysts from undersaturated tuffs and basanites, East Fife, Scotland. Journal of Petrology 17 (4), 472–498.

Chapman, N. A., Powell, R., 1976. Origin of anorthoclase megacrysts in alkali basalts. Contributions to Mineralogy and Petrology 58 (1), 29–35.

Colvine, R. J. L., 1968. Pyrope from Elie, Fife. Scottish Journal of Geology 4, 283–286.

Cortés, J. A., Smith, E. I., Valentine, G. A., Johnsen, R., Rasoazanamparany, C., Widom, E., Sas, M., Ruth, D., 2015. Intrinsic conditions of magma genesis at the Lunar Crater Volcanic Field (Nevada), and implications for internal plumbing and magma ascent. American Mineralogist 100 (2-3), 396–413.

Dickey, J. S., 1968. Eclogitic and other inclusions in the mineral breccia member of the Deborah Volcanic Formation at Kakanui, New Zealand. American Mineralogist 53, 1304–1319.

Donaldson, C. H., 1984. Kinetics of pyrope megacryst reactions in ascending basaltic magma –relevance to high-pressure magmatic crystallization at Elie Ness, East Fife. Geological Magazine 121 (06), 615–620.

Du Bray, E. A., Ludington, S. D., Brooks, W. E., Gamble, B. M., Ratte, J. C., Richter, D. H., Soria-Escalante, E., 1995. Compositional characteristics of middle to upper Tertiary volcanic rocks of the Bolivian Altiplano. U.S. Geological Survey Bulletin 2119.

Duda, A., Schmincke, H. U., 1985. Polybaric differentiation of alkali basaltic magmas: evidence from green-core clinopyroxenes (Eifel, FRG). Contributions to Mineralogy and Petrology 91 (4), 340–353.

Elburg, M. A., Soesoo, A., 1999. Jurassic alkali-rich volcanism in Victoria (Australia): lithospheric versus asthenospheric source. Journal of African Earth Sciences 29 (1), 269–280.

Elliott, H., 2015. Pb-Zn mineralization within the Limerick Basin (SW Ireland): A role for volcanism? Ph.D. thesis, University of Southampton.

Elliott, H. A. L., Gernon, T. M., Roberts, S., Hewson, C., 2015. Basaltic maar-diatreme volcanism in the Lower Carboniferous of the Limerick Basin (SW Ireland). Bulletin of Volcanology 77 (5), 1–22.

Fitton, J. G., Saunders, A. D., Norry, M. J., Hardarson, B. S., Taylor, R. N., 1997. Thermal and chemical structure of the Iceland plume. Earth and Planetary Science Letters 153 (3–4), 197–208.

Fodor, R. V., Dobosi, G., Sial, A. N., 1995. Zoned clinopyroxenes in alkalic basalt: Clues to fractionation and magma-mixing histories for seemingly primitive magmas. Chemie der Erde 55, 133–148.

Francis, E. H., Hopgood, A. M., 1970. Volcanism and the Ardross Fault, Fife. Scottish Journal of Geology 6 (2), 162–185.

Gernon, T. M., Gilbertson, M. A., Sparks, R. S. J., Field, M., 2009. The role of

gas-fluidisation in the formation of massive volcaniclastic kimberlite. Lithos 112S, 439–451.
Gernon, T. M., Upton, B. G. J., Hincks, T. K., 2013. Eruptive history of an alkali basaltic diatreme from Elie Ness, Fife, Scotland. Bulletin of Volcanology 75 (5), 704.
Hinton, R. W., Upton, B. G. J., 1991. The chemistry of zircon: Variations within and between large crystals from syenite and alkali basalt xenoliths. Geochimica et Cosmochimica Acta 55 (11), 3287–3302.
Hirose, K., Kushiro, I., 1993. Partial melting of dry peridotites at high pressures: Determination of compositions of melts segregated from peridotite using aggregates of diamond. Earth and Planetary Science Letters 114 (4), 477–489.
Imai, N., Terashima, S., Itoh, S., Ando, A., 1995. 1994 compilation of analytical data for minor and trace elements in seventeen GSJ geochemical reference samples, "Igneous rock series". Geostandards Newsletter 19, 135–213.
Irving, A. J., Frey, F. A., 1984. Trace element abundances in megacrysts and their host basalts: Constraints on partition coefficients and megacryst genesis. Geochimica et Cosmochimica Acta 48 (6), 1201–1221.
Jankovics, M. É., Harangi, S., Kiss, B., Ntaflos, T., 2012. Open-system evolution of the Füzes-tó alkaline basaltic magma, western Pannonian Basin: Constraints from mineral textures and compositions. Lithos 140–141, 25–37.
Jelsma, H., Barnett, W., Richards, S., Lister, G., 2009. Tectonic setting of kimberlites. Lithos 112, S1, 155–165.
Kuo, L. C., Kirkpatrick, R. J., 1985. Dissolution of mafic minerals and its implications for the ascent velocities of peridotite-bearing basaltic magmas. The Journal of Geology 93 (6), 691–700.
Kurszlaukis, S., Barnett, W. P., 2003. Volcanological and structural aspects of the Venetia kimberlite cluster - a case study of South African kimberlite maar-diatreme volcanoes. South African Journal of Geology 106, 165–192.
Le Roex, A. P., Bell, D. R., Davis, P., 2003. Petrogenesis of Group I Kimberlites from Kimberley, South Africa: Evidence from bulk-rock geochemistry. Journal of Petrology 44 (12), 2261–2286.
Leat, P. T., Jackson, S. E., Thorpe, R. S., Stillman, C. J., 1986. Geochemistry of bimodal basalt-subalkaline/peralkaline rhyolite provinces within the Southern British Caledonides. Journal of the Geological Society 143 (2), 259–273.
Lorenz, V., 1986. On the growth of maars and diatremes and its relevance to the formation of tuff rings. Bulletin of Volcanology 48, 265–274.
Lorenz, V., Kurszlaukis, S., 2007. Root zone processes in the phreatomagmatic pipe emplacement model and consequences for the evolution of maar–diatreme volcanoes. Journal of Volcanology and Geothermal Research 159 (1-3), 4–32.
Macdonald, R., Gottfried, D., Farrington, M. J., Brown, F. W., Skinner, N. G., 1981. Geochemistry of a continental tholeiite suite: late Palaeozoic quartz

651 dolerite dykes of Scotland. Earth and Environmental Science Transactions
652 of the Royal Society of Edinburgh 72, 57–74.
653 Mattsson, H. B., Tripoli, B. A., 2011. Depositional characteristics and volcanic
654 landforms in the Lake Natron–Engaruka monogenetic field, northern Tan-
655 zania. Journal of Volcanology and Geothermal Research 203 (1–2), 23–34.
656 McDonough, W. F., Sun, S., 1995. The composition of the Earth. Chemical
657 Geology 120, 223–253.
658 Meschede, M., 1986. A method of discriminating between different types of
659 mid-ocean ridge basalts and continental tholeiites with the Nb-Zr-Y dia-
660 gram. Chemical Geology 56, 207–218.
661 Monaghan, A. A., Pringle, M. S., 2004. $^{40}Ar/^{39}Ar$ geochronology of
662 Carboniferous-Permian volcanism in the Midland Valley, Scotland. Geo-
663 logical Society, London, Special Publications 223 (1), 219–241.
664 Montagna, C. P., Papale, P., Longo, A., 2015. Timescales of mingling in shal-
665 low magmatic reservoirs. Geological Society, London, Special Publications
666 422, 131–140.
667 Morimoto, N., Fabries, J., Ferguson, A. K., Ginzburg, I. V., Ross, M., Seifert,
668 F. A., Zussman, J., Aoki, K., Gottardi, G., 1988. Nomenclature of pyroxenes.
669 American Mineralogist 73, 1123–1133.
670 Murton, B., Taylor, R., Thirlwall, M., 2002. Plume-ridge interaction: A
671 geochemical perspective from the Reykjanes Ridge. Journal of Petrology
672 43 (11), 1987–2012.
673 Nimis, P., 1995. A clinopyroxene geobarometer for basaltic systems based
674 on crystal-structure modeling. Contributions to Mineralogy and Petrology
675 121 (2), 115–125.
676 Nimis, P., Taylor, R. W., 2000. Single clinopyroxene thermobarometry for
677 garnet peridotites. Part I. Calibration and testing of a Cr-in-Cpx barome-
678 ter and an enstatite-in-Cpx thermometer. Contributions to Mineralogy and
679 Petrology 139 (5), 541–554.
680 Nimis, P., Ulmer, P., 1998. Clinopyroxene geobarometry of magmatic rocks
681 Part 1: An expanded structural geobarometer for anhydrous and hydrous,
682 basic and ultrabasic systems. Contributions to Mineralogy and Petrology
683 133 (1), 122–135.
684 Parfitt, E. A., 2004. A discussion of the mechanisms of explosive basaltic
685 eruptions. Journal of Volcanology and Geothermal Research 134 (1–2), 77–
686 107.
687 Pe-Piper, G., 1984. Zoned pyroxenes from shoshonite lavas of Lesbos, Greece:
688 Inferences concerning shoshonite petrogenesis. Journal of Petrology 25 (2),
689 453–472.
690 Putirka, K., Johnson, M., Kinzler, R., Longhi, J., Walker, D., 1996. Thermo-
691 barometry of mafic igneous rocks based on clinopyroxene-liquid equilibria,
692 0–30 kbar. Contributions to Mineralogy and Petrology 123 (1), 92–108.
693 Putirka, K. D., 2008. Thermometers and barometers for volcanic systems.
694 Reviews in Mineralogy and Geochemistry 69 (1), 61–120.
695 Putirka, K. D., Mikaelian, H., Ryerson, F., Shaw, H., 2003. New clinopyroxene-

liquid thermobarometers for mafic, evolved, and volatile-bearing lava compositions, with applications to lavas from Tibet and the Snake River Plain, Idaho. American Mineralogist 88 (10), 1542–1554.
Ronga, F., Lustrino, M., Marzoli, A., Melluso, L., 2009. Petrogenesis of a basalt-comendite-pantellerite rock suite: the Boseti Volcanic Complex (Main Ethiopian Rift). Mineralogy and Petrology 98 (1), 227–243.
Rooney, T. O., Bastow, I. D., Keir, D., 2011. Insights into extensional processes during magma assisted rifting: Evidence from aligned scoria cones. Journal of Volcanology and Geothermal Research 201 (1–4), 83–96.
Smedley, P. L., 1988. Trace element and isotopic variations in Scottish and Irish Dinantian volcanism: Evidence for an OIB-like mantle source. Journal of Petrology 29 (2), 413–443.
Son, M., Kim, J. S., Jung, S., Ki, J. S., Kim, M.-C., Sohn, Y. K., 2012. Tectonically controlled vent migration during maar–diatreme formation: An example from a Miocene half-graben basin in SE Korea. Journal of Volcanology and Geothermal Research 223–224, 29–46.
Sparks, R. S. J., Baker, L., Brown, R., Field, M., Schumacher, J., Stripp, G., Walters, A., 2006. Dynamical constraints on kimberlite volcanism. Journal of Volcanology and Geothermal Research 155, 18–48.
Stoppa, F., 1996. The San Venanzo maar and tuff ring, Umbria, Italy: eruptive behaviour of a carbonatite-melilitite volcano. Bulletin of Volcanology 57 (7), 563–577.
Stoppa, F., Lloyd, F. E., Rosatelli, G., 2003. CO_2 as the propellant of carbonatite-kamafugite cognate pairs and the eruption of diatremic tuffisite. Periodico di Mineralogia 72, 205–222.
Streck, M. J., 2008. Mineral textures and zoning as evidence for open system processes. Mineralogical Society of America 69 (1), 595–622.
Streck, M. J., Dungan, M. A., Malavassi, E., Reagan, M. K., Bussy, F., 2002. The role of basalt replenishment in the generation of basaltic andesites of the ongoing activity at Arenal volcano, Costa Rica: evidence from clinopyroxene and spinel. Bulletin of Volcanology 64 (5), 316–327.
Streck, M. J., Leeman, W. P., Chesley, J., 2007. High-magnesian andesite from Mount Shasta: A product of magma mixing and contamination, not a primitive mantle melt. Geology 35 (4), 351–354.
Tepley, F. J., Davidson, J. P., Tilling, R. I., Arth, J. G., 2000. Magma mixing, recharge and eruption histories recorded in plagioclase phenocrysts from El Chichón Volcano, Mexico. Journal of Petrology 41 (9), 1397–1411.
Ubide, T., Galé, C., Larrea, P., Arranz, E., Lago, M., 2014. Antecrysts and their effect on rock compositions: The Cretaceous lamprophyre suite in the Catalonian Coastal Ranges (NE Spain). Lithos 206-207, 214–233.
Upton, B. G. J., Aspen, P., Rex, D. C., Melcher, F., Kinny, P., 1998. Lower crustal and possible shallow mantle samples from beneath the Hebrides: evidence from a xenolithic dyke at Gribun, western Mull. Journal of the Geological Society 155 (5), 813–828.
Upton, B. G. J., Finch, A. A., Słaby, E., 2009. Megacrysts and salic xenoliths in

741 Scottish alkali basalts: derivatives of deep crustal intrusions and small-melt
742 fractions from the upper mantle. Mineralogical Magazine 73 (6), 943–956.
743 Upton, B. G. J., Hinton, R. W., Aspen, P., Finch, A., Valley, J. W., 1999.
744 Megacrysts and associated xenoliths: Evidence for migration of geochem-
745 ically enriched melts in the upper mantle beneath Scotland. Journal of
746 Petrology 40 (6), 935–956.
747 Upton, B. J. G., Aspen, P., Chapman, N. A., 1983. The upper mantle and
748 deep crust beneath the British Isles: evidence from inclusions in volcanic
749 rocks. Journal of the Geological Society 140 (1), 105–121.
750 Upton, B. G. J., Aspen, P., Hinton, R. W., 2003. Garnet pyroxenite xeno-
751 liths and pyropic megacrysts in Scottish alkali basalts. Scottish Journal of
752 Geology 39, 169–184.
753 Upton, B. G. J., Downes, H., Kirstein, L. A., Bonadiman, C., Hill, P. G., Ntaf-
754 los, T., 2011. The lithospheric mantle and lower crust–mantle relationships
755 under Scotland: a xenolithic perspective. Journal of the Geological Society
756 168, 873–886.
757 Wallis, S., 1989. Petrology and geochemistry of Late Carboniferous-Early Per-
758 mian volcanic rocks of Scotland. Ph.D. thesis, University of Edinburgh.
759 Wass, S. Y., 1979. Multiple origins of clinopyroxenes in alkali basaltic rocks.
760 Lithos 12 (2), 115–132.
761 White, J. D. L., Ross, P. S., 2011. Maar-diatreme volcanoes: A review. Journal
762 of Volcanology and Geothermal Research 201 (1–4), 1–29.
763 Wilson, M., Neumann, E. R., Davies, G. R., Timmerman, M. J., Heeremans,
764 M., Larsen, B. T., 2004. Permo-Carboniferous magmatism and rifting in Eu-
765 rope: introduction. Geological Society, London, Special Publications 223 (1),
766 1–10.
767 Winchester, J., Floyd, P., 1977. Geochemical discrimination of different
768 magma series and their differentiation products using immobile elements.
769 Chemical Geology 20, 325 – 343.
770 Yücel, C., Arslan, M., Temizel, İ., Abdioğlu, E., 2014. Volcanic facies and
771 mineral chemistry of Tertiary volcanics in the northern part of the East-
772 ern Pontides, northeast Turkey: implications for pre-eruptive crystalliza-
773 tion conditions and magma chamber processes. Mineralogy and Petrology
774 108 (3), 439–467.
775 Zajacz, Z., Kovács, I., Szabó, C., Halter, W., Pettke, T., 2007. Evolution of
776 mafic alkaline melts crystallized in the uppermost lithospheric mantle: a
777 melt inclusion study of olivine-clinopyroxenite xenoliths, Northern Hungary.
778 Journal of Petrology 48 (5), 853–883.
779 Zhang, H.-F., Ying, J.-F., Shimoda, G., Kita, N. T., Morishita, Y., Shao,
780 J.-A., Tang, Y.-J., 2007. Importance of melt circulation and crust-mantle
781 interaction in the lithospheric evolution beneath the North China Craton:
782 Evidence from Mesozoic basalt-borne clinopyroxene xenocrysts and pyrox-
783 enite xenoliths. Lithos 96 (1–2), 67–89.
784 Zhu, Y., Ogasawara, Y., 2004. Clinopyroxene phenocrysts (with green salite
785 cores) in trachybasalts: implications for two magma chambers under the

Kokchetav UHP massif, North Kazakhstan. Journal of Asian Earth Sciences 22 (5), 517–527.

Figure Captions

Figure 1 | **a.** Inset map of Scotland showing location of east Fife. **b.** Simplified geological map of east Fife showing the main diatremes and intrusions, including Elie Ness (EN) and Elie Harbour (EH) (Lst.: limestone; Sst.: sandstone). **c.** Geological map of the Elie Ness diatreme showing stratigraphy and three lithofacies associations (modified after Gernon et al., 2013). Sample numbers, shown in circles, correspond to sampled locality; note that blue circles signify sampled dykes; numbers shown in red signify samples also used for pyroxene analysis; these were collected from pyroclastic deposits (1L, 5, 14), a basanitic breccia pipe (10) and a trachybasaltic dyke (17). Sample 8 is a tuff from a small neighbouring diatreme ∼150 m to the east (not shown). Location of sample 1L is approximate.

Figure 2 | **a.** TAS classification of selected volcanic rocks from Elie Ness (Table 1), plotted alongside published compositions of similar alkaline volcanic rocks in Scotland, of Lower Carboniferous (Smedley, 1988), Upper Carboniferous (Macdonald et al., 1981), and Permo-Carboniferous* (Wallis, 1989) age, and nearby diatremes in east Fife (Chapman, 1976). **b.** Classification of the Elie Ness volcanic rocks using the Nb/Y vs. Zr/TiO_2 diagram of Winchester and Floyd (1977), plotted alongside other Scottish volcanics (Smedley, 1988; Wallis, 1989). *Please note that these represent mean values (see Table 5.1 of Wallis, 1989).

Figure 3 | **a.** Zr–Nb plot (*sensu* Leat et al., 1986) showing the composition of all Elie Ness volcanic rocks (Tables 1 & 2) determined in this study. For comparison, the compositions of similar diatremes in Limerick, Ireland (Elliott, 2015) and Permo-Carboniferous alkaline volcanics in Scotland (Smedley, 1988; Wallis, 1989) are also shown. **b.** Zr/Y vs. Nb/Y plot (*sensu* Fitton et al., 1997) comparing Elie Ness basalts with alkali basalts from the Scottish and Irish Carboniferous (see (a) for key to symbols). Fractional melting curves are shown for spinel and garnet lherzolite according to Fitton et al. (1997).

Figure 4 | **a–c.**: C1 chondrite normalised (McDonough and Sun, 1995) REE plots for LFAs 1–3. **d–f.**: Primitive mantle-normalised (McDonough and Sun, 1995) multi-trace element distribution diagrams.

Figure 5 | Field photographs of (**a**) a pyrope megacryst from Elie Ness (© BGS); (**b**) pyroxenitic cumulate, and (**c**) pyroxenite megacryst coated in a thin layer of juvenile vesicular basalt. All these features occur within a ∼65

m thick sequence of pyroclastic (lapilli) tuffs of the Elie Ness diatreme (see Gernon et al., 2013).

Figure 6 | Photomicrographs of cumulate nodules from the Elie Ness diatreme (photomicrographs are ∼2.2 mm wide). **a.** Coarse kaersutite (Kt) pyroxenite comprising idiomorphic augite (Au) prisms up to 3 mm with patchy zonation; **b.** amphibole pyroxenite comprising ∼50% idiomorphic to subhedral amphibole (<2 mm), augite (pale dull green and present as small "granulated" crystals) and interstitial chlorite (Ch) (after glass) with quench feldspar and spherical globules of calcite surrounded by chlorite; **c.** sub-spherical 'ocelli' of calcite (Ca) with chloritic rims within a coarse amphibole pyroxenite; **d.** coarse-grained biotite pyroxenite comprising colourless augite and subhedral biotite (Bt); **e.** amphibole pyroxenite containing large (up to 3 mm) subhedral pyroxenes with oscillatory zoning, neoblast-type augites, anhedral kaersutite, possible pseudomorphs after olivine, and anhedral late-stage oligoclase ($An_{10.2}Ab_{84.8}Or_{5.0}$—$An_{12.5}Ab_{83.2}Or_{4.3}$); **f.** Idiomorphic augite exhibiting hourglass zoning within a coarse amphibole pyroxenite (same sample as (c) above).

Figure 7 | Clinopyroxene classification diagram (Morimoto et al., 1988) of sampled volcanic rocks from Elie Ness (see Fig. 1c for locations).

Figure 8 | Zoning profiles showing compositional variations within a clinopyroxene crystal (S17-40) from a trachybasaltic dyke (S17, see Fig. 1c); backscattered electron image; note: c = core, r = rim.

Figure 9 | Plots **a.**–**e.** correspond to pyroxene analyses (n = 634); **a.** CaO vs. Al_2O_3 plotted for pyroxenes from three samples of pyroclastic lapilli tuffs from different locations across the diatreme (see Fig. 1c), a basanite dyke and a breccia pipe (see Fig. 1c); also plotted are the compositions of pyroxenitic cumulates and clinopyroxene crystals from Chapman (1974b), and clinopyroxene megacrysts and xenoliths from Highland intrusions described by Wallis (1989); **b.** TiO_2 vs. Al_2O_3; **c.** Al_2O_3 vs. SiO_2; **d.** Na_2O vs. Al_2O_3; **e.** MgO vs. FeO. Plot **f.** showing Na_2O vs. K_2O, is from alkali feldspars in a sample of lapilli tuff (S1L; Fig. 1b).

Figure 10 | Clinopyroxene compositions of selected volcanic rocks from Elie Ness (see Fig. 1c); **a.** Mg# vs. Cr_2O_3 (wt.%) and **b.** TiO_2 (wt.%), and **c.** Ti (apfu) vs. Al (apfu); **d.**–**f.** plot the same variables as **a.**–**c.**, above, however discriminate the cores (filled symbols, N = 33) and rims (empty symbols, N = 33) of all zoned clinopyroxene crystals (note the change in symbols); **e.** provides several examples of zoned clinopyroxene crystals and their corresponding compositions. Note that for S5, N = 2; S10, N = 17, S14, N = 5; and S17, N = 9.

Figure 11 | Cartoon illustrating the deep crustal structure beneath the Midland Valley of Scotland during late Carboniferous to Permian times. (1)

Basaltic parent melt rises from the asthenospheric mantle (∼60–70 km), crystallising high-pressure phenocrysts including pyrope garnets, and rapidly ascends to the surface, possibly exploiting lithospheric structures. (2) These magmas then incorporate trapped 'anorthoclasite suite' pegmatites, representing small fraction melts from large volumes of mantle peridotite. (3) Fuelled by CO_2 exsolution, the 'mixed' magma rises rapidly entraining xenoliths of lower crustal granulite facies metabasic lithologies, whilst also flushing out pockets of magma that had been equilibrating at lower pressures—principally between 22–28 km. (4) The magma erupts explosively forming a maar-diatreme, driven by magmatic volatiles and later influenced by interaction with meteoric water giving rise to phreatomagmatic explosions. Note GM: geophysical Moho; PM: petrological Moho.

Figure 12 | Schematic summary of the structure and lithofacies associations of the Elie Ness maar-diatreme, highlighting the key depositional processes and geochemical relationships between the major units; modified after Gernon et al. (2013).

Supplementary Figure Captions

Figure S1 | Backscattered electron (BSE) images (taken with a Cameca SX100 electron microprobe) of zoned clinopyroxene crystals from samples 5, 10 and 17 (sample numbers shown, see Fig. 1c for locations); note the zoning traverses shown correspond to Mg# profiles in Fig. S2. The horizontal scale bar beneath each image is 100 μm.

Figure S2 | Normalised zoning profiles showing variations in Mg# across clinopyroxene crystals depicted in Fig. S1 (note there are no images for S10-18 and S17-81).

Tables

Sample No.	S1	S5	S8	S10	S17	JA-2	JA-2	BRR-1	BRR-2
Lithofacies	Lapilli tuff	Lapilli tuff	Lapilli tuff	Breccia Pipe	Dyke	Measured	Recom. value	Measured	(Murton et al. 2002)
(Wt.%)	LFA 1	LFA 2	Vent to east	LFA 3	LFA 3				
SiO2	50.19	46.33	48.86	45.29	46.72	-	-	49.28	49.82
TiO2	2.16	2.26	2.27	2.77	2.39	-	-	1.02	1.03
Al2O3	13.56	14.74	12.23	14.07	13.54	-	-	14.37	14.37
Fe2O3	12.39	14.37	12.33	13.45	13.29	-	-	11.67	11.88
MnO	0.25	0.20	0.17	0.47	0.37	-	-	0.19	0.18
MgO	9.96	8.75	9.39	9.38	10.86	-	-	8.49	8.57
CaO	6.32	6.97	10.50	8.70	7.08	-	-	11.74	11.95
Na2O	1.98	1.33	2.00	1.26	1.92	-	-	1.92	1.97
K2O	2.80	3.32	1.37	4.09	3.37	-	-	0.05	0.05
P2O5	0.47	0.69	0.59	0.62	0.53	-	-	0.08	0.09
Total	100.07	98.97	99.70	100.09	100.07	-	-	-	-
LOI	9.52	9.54	12.41	4.23	4.57	-	-	-	-
(ppm)									
Li	32.5	20.1	31.3	17.7	21.7	28.9	27.3	5.16	5.40
Sc	19.6	19.4	17.4	22.5	21.1	17.9	19.6	43.98	45.87
Rb	49.0	50.6	34.0	25.3	46.6	76.7	72.9	0.56	0.60
Sr	260	418	156	504	486	243	248	69.00	71.20
Y	26.7	32.0	26.5	25.1	21.4	17.4	18.3	27.71	27.40
Zr	233.5	304.1	230.1	238.5	215.0	119.3	116.0	55.22	54.90
Nb	50.6	70.4	50.9	59.6	53.4	8.8	9.5	1.05	1.19
Cs	2.34	2.10	1.18	1.81	1.32	5.16	4.60	0.01	0.01
Ba	490	340	278	703	942	319	321	6.85	6.55
La	45.40	51.27	46.94	37.62	33.78	16.03	15.80	1.54	1.62
Ce	87.60	104.70	90.08	74.12	66.56	33.31	32.70	5.10	5.39
Pr	10.23	11.81	10.40	8.93	7.99	3.82	3.84	0.98	1.01
Nd	39.25	44.95	39.83	35.68	31.76	14.41	13.90	5.71	5.68
Sm	7.63	8.64	7.80	7.54	6.61	3.14	3.11	2.29	2.17
Eu	2.19	2.54	2.33	2.40	2.10	0.91	0.93	0.86	0.81
Gd	6.58	7.51	6.87	6.87	5.94	3.05	3.06	3.43	3.25
Tb	0.94	1.10	0.97	0.96	0.83	0.48	0.44	0.64	0.63
Dy	5.10	6.03	5.14	5.09	4.42	2.92	2.80	4.35	4.26
Ho	0.95	1.12	0.93	0.91	0.78	0.60	0.50	0.97	0.98
Er	2.44	2.83	2.31	2.23	1.89	1.70	1.48	2.88	2.86
Tm	0.34	0.38	0.31	0.29	0.25	0.25	0.28	0.44	0.43
Yb	2.08	2.34	1.81	1.75	1.49	1.70	1.62	2.91	2.79
Lu	0.30	0.33	0.25	0.25	0.20	0.26	0.27	0.45	0.44
Hf	5.29	6.09	5.13	5.16	4.60	2.94	2.86	1.56	1.55
Ta	3.20	4.57	3.43	3.95	3.47	0.75	0.80	2.50	0.06
Pb	14.09	7.73	9.60	12.73	4.56	22.28	19.20	0.34	0.38
Th	8.02	8.00	5.61	4.76	4.24	4.88	5.03	0.07	0.05
U	1.80	2.04	1.74	1.26	1.20	2.24	2.21	0.04	0.04

Table 1
Major and trace element data for selected Elie Ness volcanics, samples 1, 5, 8, 10 & 17 (see Fig. 1c for locations). Major elements measured by XRF and trace elements by ICP-MS at the University of Southampton (see methods). Analyses of International standard JA-2 (Imai et al., 1995) and Southampton internal basalt standard BRR-1 (Murton et al., 2002) are presented with consensus values for these rocks. Further whole-rock analyses of comparable volcanics in this area are reported in Table 5.1 (and the appendix) of Wallis (1989).

Sample No.	S2	S3	S4	S6	S9	S11	S12	S14	S15	S16	S18	S19	S20	JA-2	JA-2	BRR-1	BRR-2
Lithofacies	LFA1	LFA1	LFA1	LFA1	LFA3	LFA2	LFA2	LFA2	LFA2	LFA3	LFA2	LFA2	LFA2	Measured	Recom. value	Measured	(Murton et al. 2002)
(ppm)																	
Li	30.27	22.38	11.90	13.31	19.49	15.42	19.53	15.50	19.82	16.96	29.31	21.82	25.75	28.88	27.30	5.16	5.40
Sc	16.29	19.98	6.73	12.20	5.35	16.76	15.54	16.98	17.68	10.03	16.81	17.16	18.20	17.86	19.60	43.98	45.87
Rb	39.77	20.05	31.46	44.14	12.11	39.42	78.17	40.91	52.18	30.44	23.46	57.15	70.70	76.70	72.90	0.56	0.60
Sr	190.10	272.40	95.79	170.60	152.00	325.20	302.30	361.70	297.90	244.90	251.30	260.80	242.10	242.80	248.00	69.00	71.20
Y	25.66	26.11	14.15	27.00	10.41	24.54	26.61	25.48	27.18	14.88	27.60	27.80	28.31	17.38	18.30	27.71	27.40
Zr	227.60	251.50	140.70	333.00	66.52	243.50	225.70	246.00	240.50	116.60	243.50	247.00	242.70	119.30	116.00	55.22	54.90
Nb	55.82	59.32	28.89	72.20	16.23	58.64	53.57	59.93	60.73	28.15	60.02	60.50	62.06	8.84	9.47	1.05	1.19
Cs	1.20	0.30	1.68	1.85	0.66	1.48	2.38	1.43	1.76	0.47	0.93	1.91	1.89	5.16	4.60	0.01	0.01
Ba	385.20	622.90	139.80	710.50	131.30	569.60	406.00	630.70	665.20	451.30	841.70	535.10	527.80	318.70	321.00	6.85	6.55
La	47.91	68.67	24.92	58.92	18.18	43.55	49.99	43.81	51.12	21.06	50.55	49.74	54.97	16.03	15.80	1.54	1.62
Ce	93.18	143.20	50.41	119.60	32.41	86.69	96.79	86.78	100.00	39.94	102.60	95.34	106.50	33.31	32.70	5.10	5.39
Pr	10.70	15.14	5.90	12.57	3.81	10.12	11.11	10.12	11.50	4.72	12.06	11.04	12.23	3.82	3.84	0.98	1.01
Nd	40.69	57.66	22.39	46.72	14.77	38.63	41.79	38.70	43.62	18.21	46.32	41.96	46.20	14.41	13.90	5.71	5.68
Sm	7.74	10.80	4.23	8.62	2.84	7.44	7.86	7.50	8.18	3.71	8.85	8.07	8.72	3.14	3.11	2.29	2.17
Eu	2.25	3.11	1.16	2.47	0.81	2.20	2.23	2.22	2.38	1.19	2.55	2.35	2.46	0.91	0.93	0.86	0.81
Gd	6.61	8.68	3.54	7.24	2.53	6.36	6.64	6.41	6.96	3.43	7.39	6.91	7.30	3.05	3.06	3.43	3.25
Tb	0.93	1.12	0.50	1.01	0.35	0.90	0.94	0.91	0.98	0.51	1.01	0.98	1.02	0.48	0.44	0.64	0.63
Dy	5.02	5.56	2.72	5.31	1.91	4.81	5.10	4.91	5.25	2.86	5.30	5.34	5.47	2.92	2.80	4.35	4.26
Ho	0.92	0.95	0.50	0.95	0.36	0.88	0.94	0.90	0.96	0.52	0.95	0.99	0.99	0.60	0.50	0.97	0.98
Er	2.36	2.25	1.29	2.34	0.93	2.20	2.41	2.29	2.43	1.30	2.41	2.51	2.52	1.70	1.48	2.88	2.86
Tm	0.32	0.29	0.18	0.32	0.13	0.30	0.33	0.31	0.33	0.17	0.32	0.35	0.35	0.25	0.28	0.44	0.43
Yb	1.97	1.72	1.11	1.94	0.74	1.84	2.07	1.90	2.03	1.02	1.94	2.12	2.12	1.70	1.62	2.91	2.79
Lu	0.28	0.24	0.16	0.27	0.11	0.26	0.29	0.27	0.29	0.14	0.27	0.30	0.30	0.26	0.27	0.45	0.44
Hf	4.84	5.35	3.07	6.37	1.48	5.05	4.99	5.20	5.11	2.64	5.15	5.35	5.16	2.94	2.86	1.56	1.55
Ta	3.00	3.77	1.89	4.69	0.66	3.65	3.58	3.71	3.71	1.67	3.78	3.92	3.95	0.75	0.80	2.50	0.06
Pb	9.15	6.73	5.39	7.45	3.48	5.22	11.81	5.31	6.11	1.56	7.84	7.92	8.03	22.28	19.20	0.34	0.38
Th	7.06	5.92	4.80	9.49	2.10	6.87	8.26	6.88	7.52	2.68	6.57	7.82	8.23	4.88	5.03	0.07	0.05
U	1.76	1.56	1.17	2.28	0.66	1.70	2.00	1.72	1.88	0.68	1.62	1.92	1.99	2.24	2.21	0.04	0.04

Table 2. Trace element data for all other Elie Ness volcanics in this study (see Fig. 1c for locations). Trace elements measured by ICP-MS at the University of Southampton (see methods). Analyses of International standard JA-2 (Imai et al., 1995) and Southampton internal basalt standard BRR-1 (Murton et al., 2002) are presented with consensus values for these rocks.

Sample	Analysis ref.	Analysis	SiO_2	TiO_2	Al2O3	Cr_2O_3	FeO	MnO	MgO	CaO	Na_2O	K_2O	Total	Mg#	Wo	En	Fs
S5	*S5-51*	Core	47.87	1.80	7.24	0.05	7.68	0.15	12.30	22.39	0.54	0.01	100.03	0.74	49.11	37.56	13.33
S5	*S5-51*	Rim	48.13	2.47	5.50	0.01	7.85	0.16	12.60	22.94	0.46	0.01	100.12	0.74	49.14	37.55	13.31
S5	*S5-15*	Crystal	47.23	2.33	7.05	0.37	7.24	0.12	12.41	21.92	0.80	0.02	99.48	0.75	48.83	38.47	12.70
S5	*S5-76*	Core	52.12	0.58	3.33	0.06	5.42	0.13	14.51	22.89	0.60	0.00	99.62	0.83	48.29	42.59	9.11
S5	*S5-76*	Rim	46.79	2.69	6.19	0.01	8.17	0.14	12.10	22.46	0.43	0.00	98.96	0.73	49.09	36.82	14.09
S10	*S10-18*	Core	50.84	0.85	4.16	0.09	9.44	0.36	11.89	20.71	1.41	0.00	99.75	0.69	46.16	36.88	16.96
S10	*S10-18*	Rim	47.46	3.24	6.34	0.02	7.85	0.18	11.92	22.28	0.77	0.24	100.31	0.73	49.40	36.78	13.81
S10	*S10-34*	Core	48.21	1.76	5.94	0.88	6.17	0.13	13.57	22.55	0.58	0.00	99.80	0.80	48.69	40.77	10.54
S10	*S10-34*	Rim	46.29	3.30	7.42	0.02	7.62	0.13	11.65	22.94	0.58	0.04	99.99	0.73	50.79	35.90	13.31
S10	*S10-56*	Core	51.36	0.82	4.27	0.39	6.67	0.16	16.44	19.57	0.65	0.00	100.32	0.81	40.98	47.91	11.11
S10	*S10-56*	Rim	46.88	2.96	6.62	0.02	7.27	0.11	12.27	23.17	0.58	0.01	99.90	0.75	50.40	37.15	12.45
S10	*S10-71*	Core	48.35	1.05	6.79	0.01	11.42	0.28	8.74	20.94	1.81	0.00	99.38	0.58	49.68	28.86	21.46
S10	*S10-71*	Rim	46.21	2.86	6.41	0.04	8.31	0.19	12.54	22.64	0.51	0.00	99.70	0.73	48.54	37.39	14.07
S10	*S10-73*	Core	49.74	1.43	4.72	0.02	10.93	0.37	9.73	20.99	1.77	0.00	99.70	0.61	48.49	31.28	20.23
S10	*S10-73*	Rim	47.08	2.62	6.45	0.01	7.82	0.17	12.88	21.86	0.58	0.04	99.52	0.75	47.55	38.99	13.46
S14	*S14-100*	Core	50.05	1.37	4.97	0.32	7.64	0.16	14.58	19.79	0.68	0.00	99.56	0.77	42.88	43.97	13.15
S14	*S14-100*	Rim	43.85	3.31	7.59	0.00	9.26	0.18	10.66	22.74	0.52	0.02	98.12	0.67	50.70	33.07	16.23
S14	*S14-65*	Core	47.52	2.19	5.98	0.78	6.50	0.12	13.27	22.40	0.47	0.00	99.22	0.78	48.68	40.15	11.16
S14	*S14-65*	Rim	44.75	3.55	7.13	0.02	8.17	0.12	12.04	22.52	0.56	0.03	98.89	0.72	49.31	36.69	14.00
S14	*S14-08*	Core	46.25	3.27	6.60	0.03	7.99	0.15	12.07	22.06	0.52	0.01	98.96	0.73	48.83	37.18	13.99
S14	*S14-08*	Rim	44.76	4.09	7.85	0.02	8.51	0.11	11.55	21.95	0.59	0.00	99.42	0.71	49.11	35.95	14.94
S14	*S14-100*	Crystal	47.82	2.32	5.84	0.00	7.45	0.18	13.02	22.25	0.57	0.00	99.44	0.76	48.09	39.14	12.77
S17	*S17-81*	Core	50.82	0.48	1.45	0.01	15.94	0.63	8.76	20.87	0.99	0.02	99.96	0.49	45.46	26.54	28.00
S17	*S17-81*	Rim	44.36	3.91	9.09	0.00	7.98	0.19	11.14	21.97	1.05	0.03	99.71	0.71	50.19	35.41	14.40
S17	*S17-12*	Core	42.99	3.67	11.07	0.08	8.33	0.14	10.68	20.99	0.77	0.01	98.73	0.70	49.48	35.05	15.47
S17	*S17-12*	Rim	49.23	1.46	13.09	0.00	5.88	0.11	6.55	12.17	3.99	1.88	94.36	0.67	46.82	35.07	18.11
S17	*S17-20*	Core	49.34	1.52	5.02	0.11	7.09	0.13	13.85	21.14	0.97	0.02	99.18	0.78	45.95	41.90	12.15
S17	*S17-20*	Rim	49.35	2.11	4.66	0.00	7.42	0.19	13.11	22.36	0.51	0.03	99.74	0.76	48.07	39.21	12.73
S17	*S17-40**	Core	47.78	2.05	7.12	0.02	8.52	0.17	11.03	22.43	0.64	0.00	99.74	0.70	50.35	34.47	15.18
S17	*S17-40**	Rim	38.30	2.55	6.30	0.01	7.36	0.20	10.70	25.11	0.46	0.04	91.02	0.72	54.96	32.58	12.46
S17	*S17-08*	Core	48.29	1.92	6.01	0.01	13.13	0.46	8.16	19.38	2.11	0.01	99.46	0.53	46.98	27.51	25.50
S17	*S17-08*	Rim	45.13	3.83	8.35	0.00	8.15	0.19	11.19	22.19	0.54	0.00	99.58	0.71	50.15	35.20	14.65
S17	*S17-50*	Crystal	50.43	1.22	4.99	0.06	7.90	0.15	13.07	20.90	0.84	0.00	99.57	0.75	46.08	40.09	13.83
S17	*S17-86*	Crystal	43.78	3.98	9.46	0.01	8.11	0.12	11.00	22.12	0.59	0.01	99.17	0.71	50.50	34.93	14.57

Table 3. Representative microprobe analysis of clinopyroxene from Elie Ness (see Fig. 1c for sample locations). Asterix denotes crystal shown in Fig. 8.

Sample	Lithofacies	Analysis ref.	Cpx-only barometer (32a); GPa	Cpx-liquid barometer (32c); GPa	Thermometer (32d); °C	KD(Fe -Mg)
E10	LFA3, breccia pipe	E10-16	0.65	1.36	1208.8	0.284
E10	LFA3, breccia pipe	E10-23a	0.98	2.07		0.283
E10	LFA3, breccia pipe	E10-36	0.61	1.70	1121.5	0.287
E10	LFA3, breccia pipe	E10-37c	0.66	1.34	1197.9	0.289
E10	LFA3, breccia pipe	E10-41	0.59	1.51	1137.5	0.288
Mean			0.7	1.60	1164.4	
STD			0.16	0.30	43.4	
E17	LFA3, dyke	E17-003	0.71	1.45	1238.4	0.287
E17	LFA3, dyke	E17-081	1.08	1.03	1136.8	0.296
Mean			0.9	1.24	1187.6	
STD			0.27	0.3	71.9	

Table 4
Quantitative pressure and temperature estimates for selected clinopyroxene crystals from Elie Ness, using the barometric and thermometric equations of Putirka (2008).

Figure 1

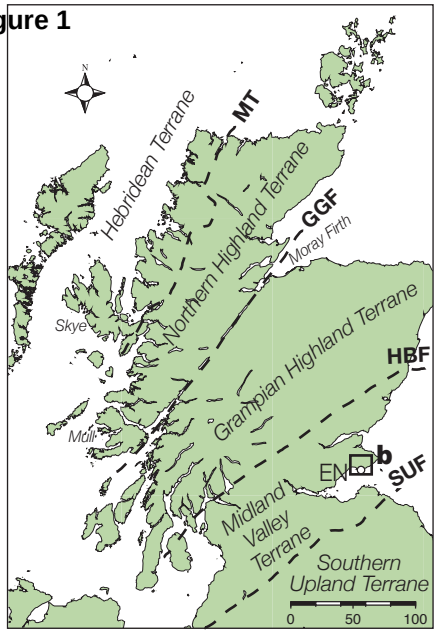
a
Hebridean Terrane
MT
Northern Highland Terrane
GGF
Moray Firth
Skye
Grampian Highland Terrane
HBF
Mdll
EN
b
SUF
Midland Valley Terrane
Southern Upland Terrane
0
50
100

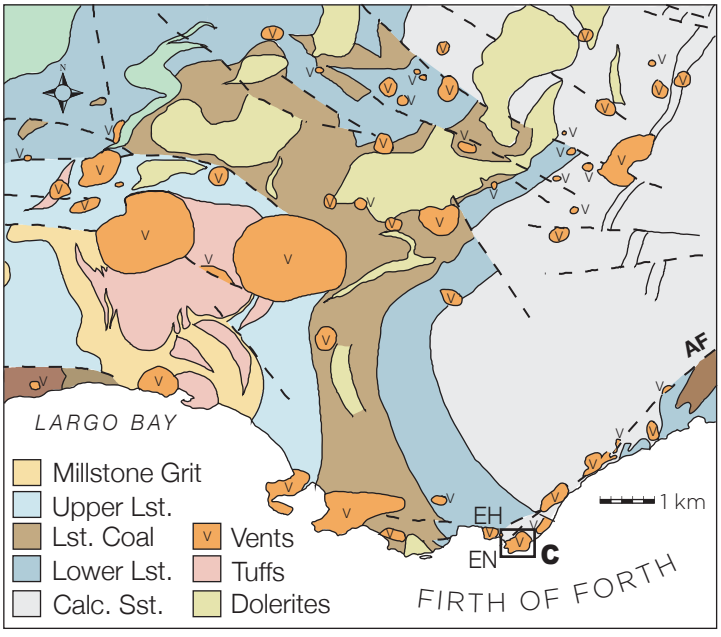
b
LARGO BAY
AF
EH
EN
c
1 km
Millstone Grit
Upper Lst.
Lst. Coal
Lower Lst.
Calc. Sst.
Vents
Tuffs
Dolerites
FIRTH OF FORTH

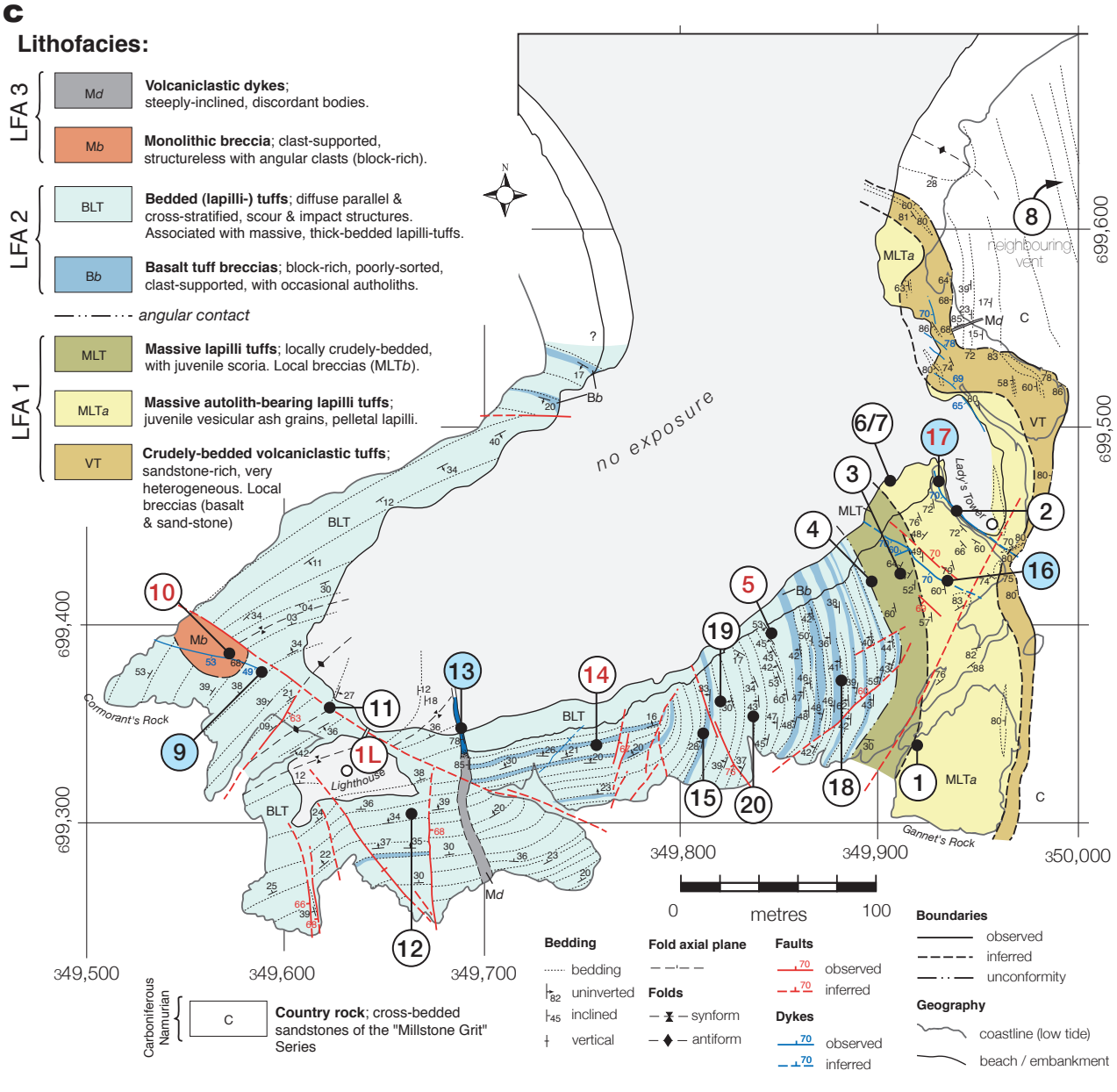
c
Lithofacies:
LFA 3
Md
Volcaniclastic dykes; steeply-inclined, discordant bodies.
Mb
Monolithic breccia; clast-supported, structureless with angular clasts (block-rich).
LFA 2
BLT
Bedded (lapilli-) tuffs; diffuse parallel & cross-stratified, scour & impact structures. Associated with massive, thick-bedded lapilli-tuffs.
Bb
Basalt tuff breccias; block-rich, poorly-sorted, clast-supported, with occasional autholiths.
angular contact
LFA 1
MLT
Massive lapilli tuffs; locally crudely-bedded, with juvenile scoria. Local breccias (MLTb).
MLTa
Massive autolith-bearing lapilli tuffs; juvenile vesicular ash grains, pelletal lapilli.
VT
Crudely-bedded volcaniclastic tuffs; sandstone-rich, very heterogeneous. Local breccias (basalt & sand-stone)
no exposure
neighbouring vent
Lady's Tower
Lighthouse
Cormorant's Rock
Gannet's Rock
699,600
699,500
699,400
699,300
349,500
349,600
349,700
349,800
349,900
350,000
0
metres
100
Bedding
bedding
uninverted
inclined
vertical
Fold axial plane
Folds
synform
antiform
Faults
observed
inferred
Dykes
observed
inferred
Boundaries
observed
inferred
unconformity
Geography
coastline (low tide)
beach / embankment
Carboniferous
Namurian
C
Country rock; cross-bedded sandstones of the "Millstone Grit" Series

Figure 2

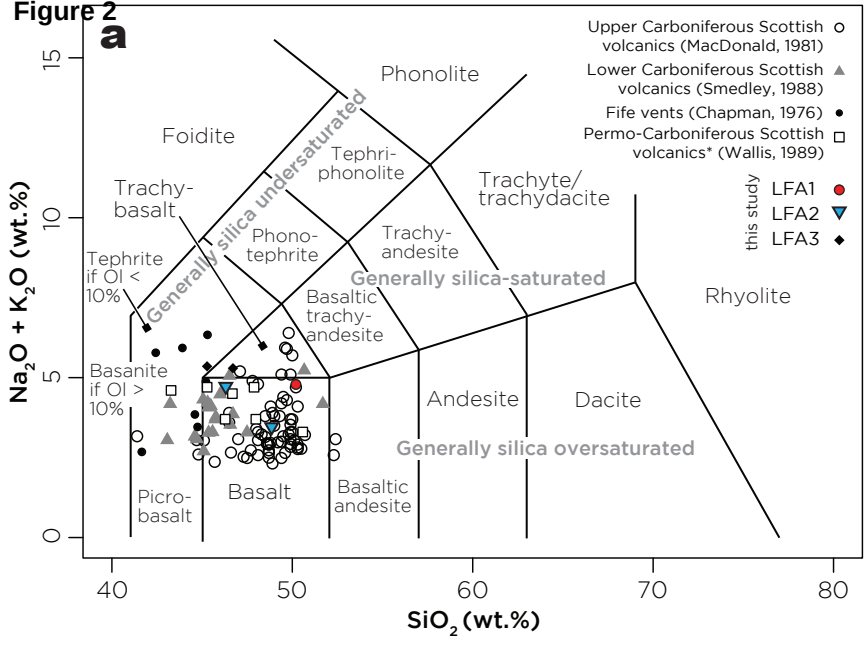
a
Upper Carboniferous Scottish volcanics (MacDonald, 1981)
Lower Carboniferous Scottish volcanics (Smedley, 1988)
Fife vents (Chapman, 1976)
Permo-Carboniferous Scottish volcanics* (Wallis, 1989)
this study
LFA1
LFA2
LFA3
Foidite
Phonolite
Tephri-phonolite
Trachyte/ trachydacite
Trachy-basalt
Phono-tephrite
Trachy-andesite
Rhyolite
Tephrite if Ol < 10%
Basanite if Ol > 10%
Basaltic trachy-andesite
Andesite
Dacite
Picro-basalt
Basalt
Basaltic andesite
Generally silica undersaturated
Generally silica-saturated
Generally silica oversaturated
Na2O + K2O (wt.%)
SiO2 (wt.%)
0
5
10
15
40
50
60
70
80

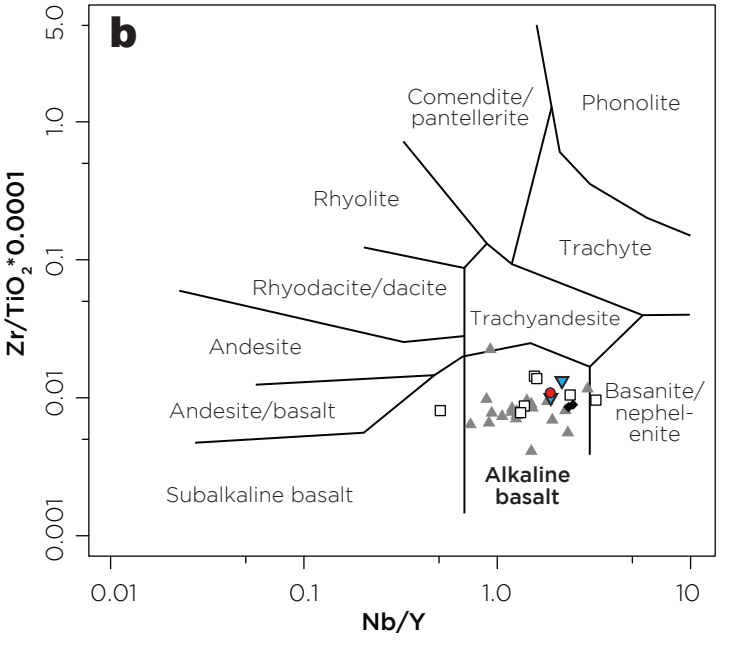
b
Comendite/ pantellerite
Phonolite
Rhyolite
Trachyte
Rhyodacite/dacite
Trachyandesite
Andesite
Andesite/basalt
Basanite/ nephel-enite
Subalkaline basalt
Alkaline basalt
Zr/TiO2*0.0001
Nb/Y
0.001
0.01
0.1
1.0
5.0
10

Figure 3

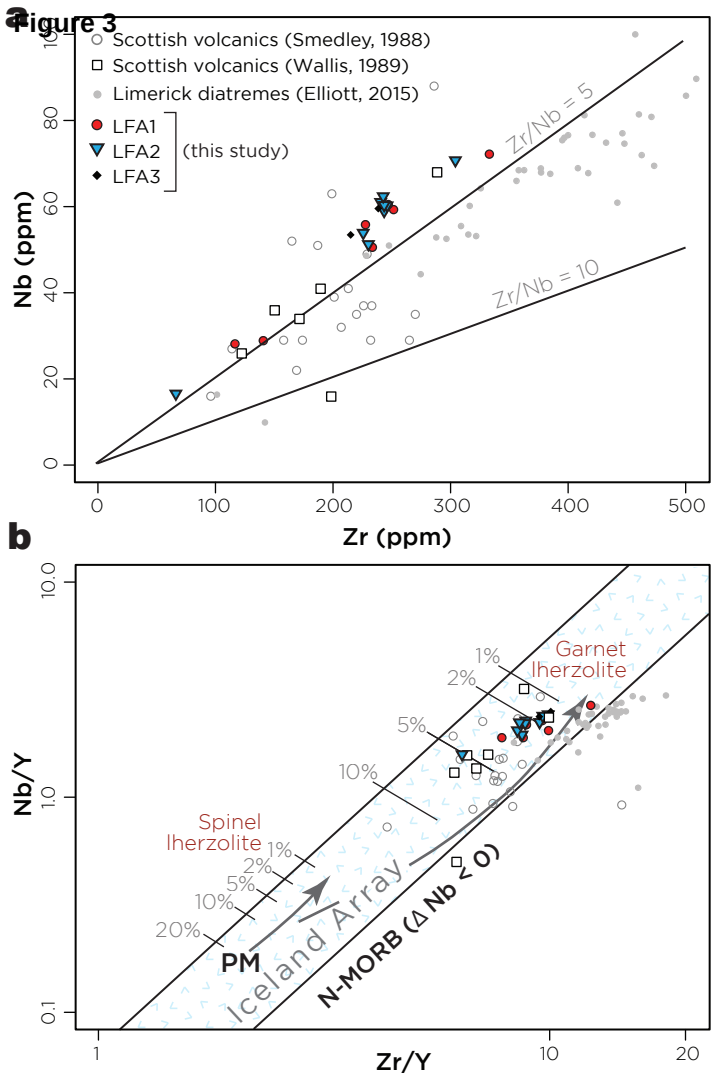
a
Scottish volcanics (Smedley, 1988)
Scottish volcanics (Wallis, 1989)
Limerick diatremes (Elliott, 2015)
LFA1
LFA2
LFA3
(this study)
Zr/Nb = 5
Zr/Nb = 10
Nb (ppm)
Zr (ppm)
0
20
40
60
80
100
0
100
200
300
400
500
b
Garnet lherzolite
Spinel lherzolite
1%
2%
5%
10%
20%
PM
Iceland Array
N-MORB (Δ Nb < 0)
Nb/Y
Zr/Y
0.1
1.0
10.0
1
10
20

Figure 4

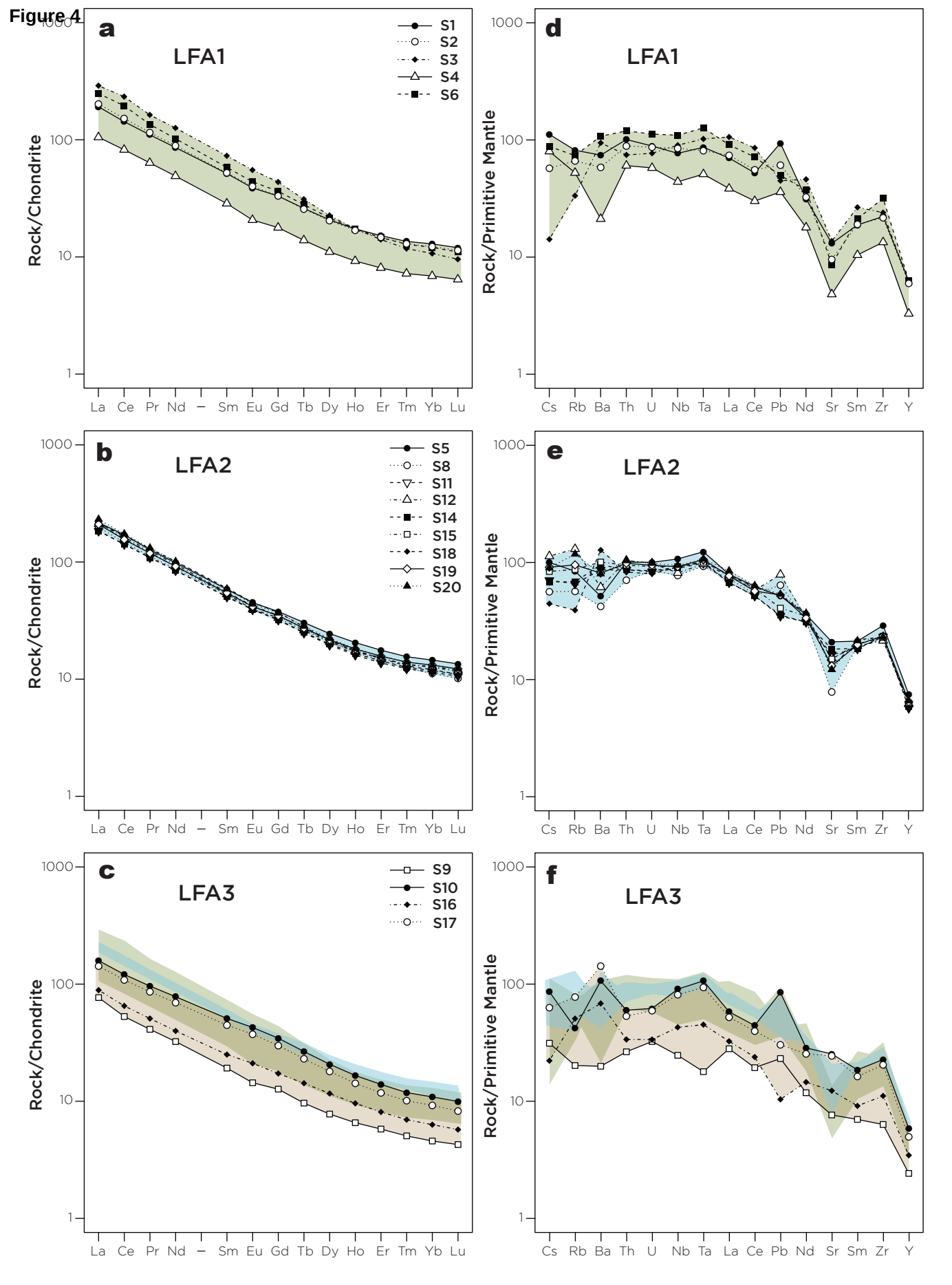
a
LFA1
S1
S2
S3
S4
S6
Rock/Chondrite
1000
100
10
1
La Ce Pr Nd – Sm Eu Gd Tb Dy Ho Er Tm Yb Lu
d
LFA1
Rock/Primitive Mantle
Cs Rb Ba Th U Nb Ta La Ce Pb Nd Sr Sm Zr Y
b
LFA2
S5
S8
S11
S12
S14
S15
S18
S19
S20
e
LFA2
c
LFA3
S9
S10
S16
S17
f
LFA3

Figure 5

Click here to download high resolution image

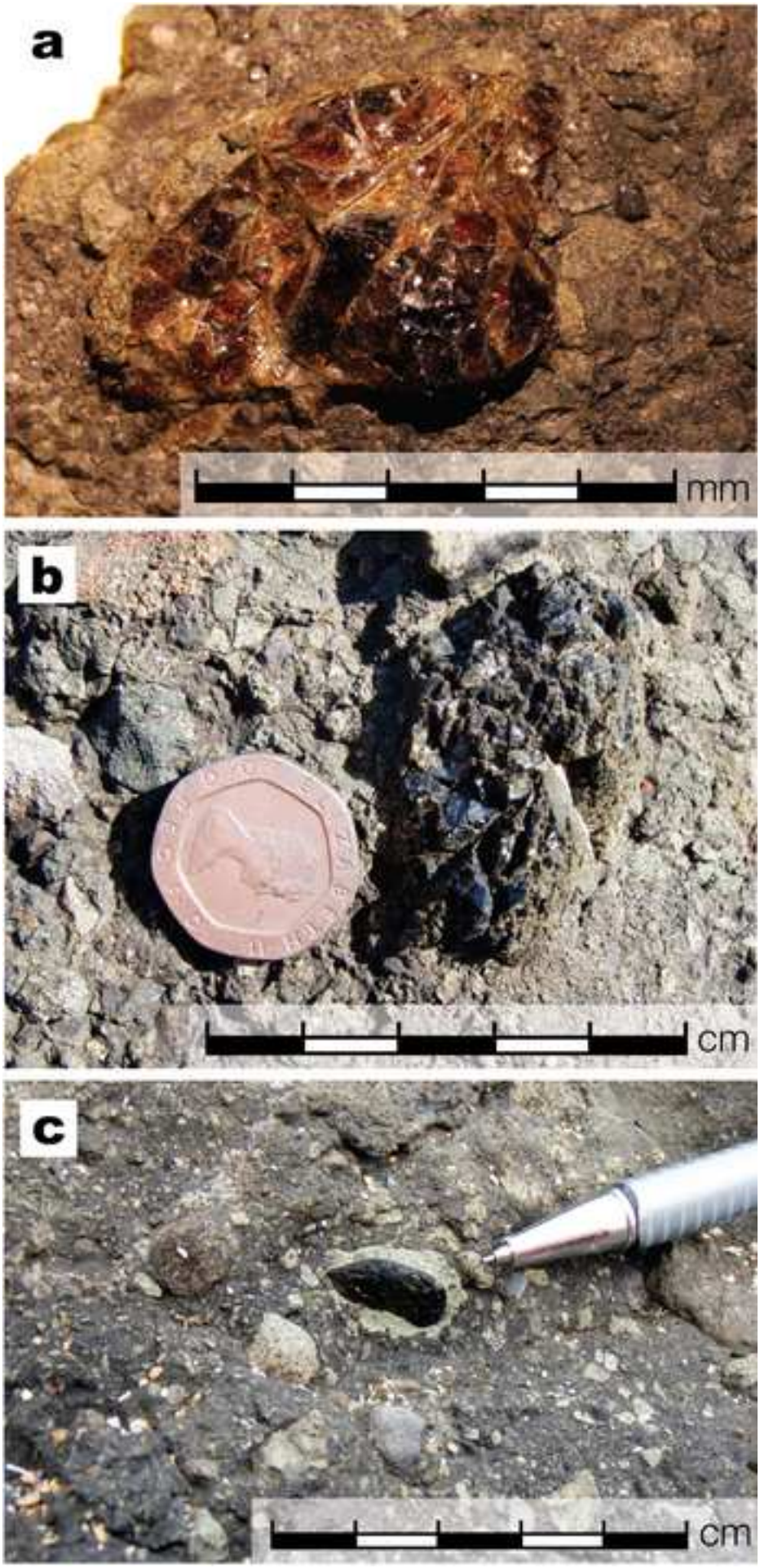

Figure 6

Click here to download high resolution image

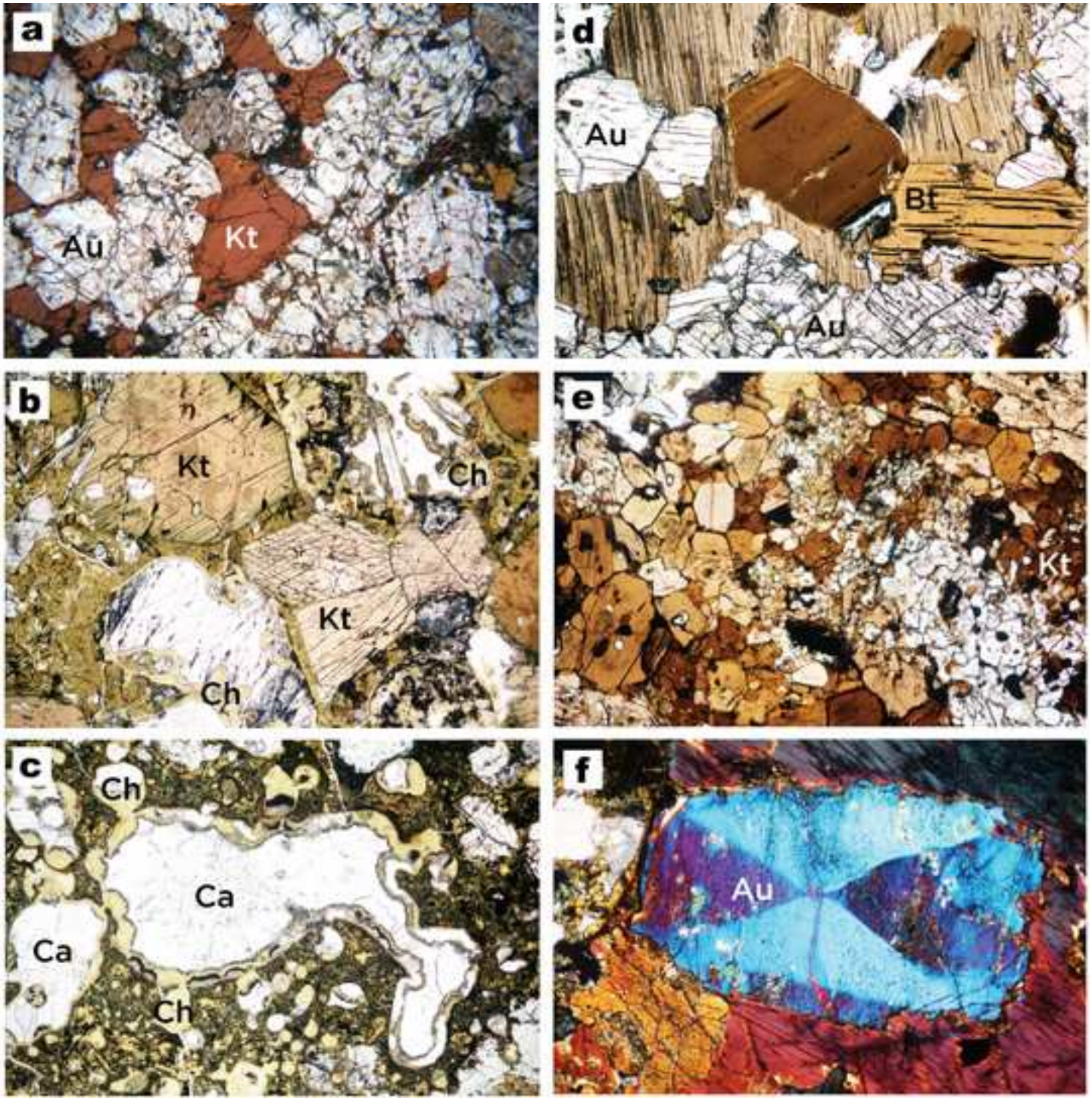

Figure 7

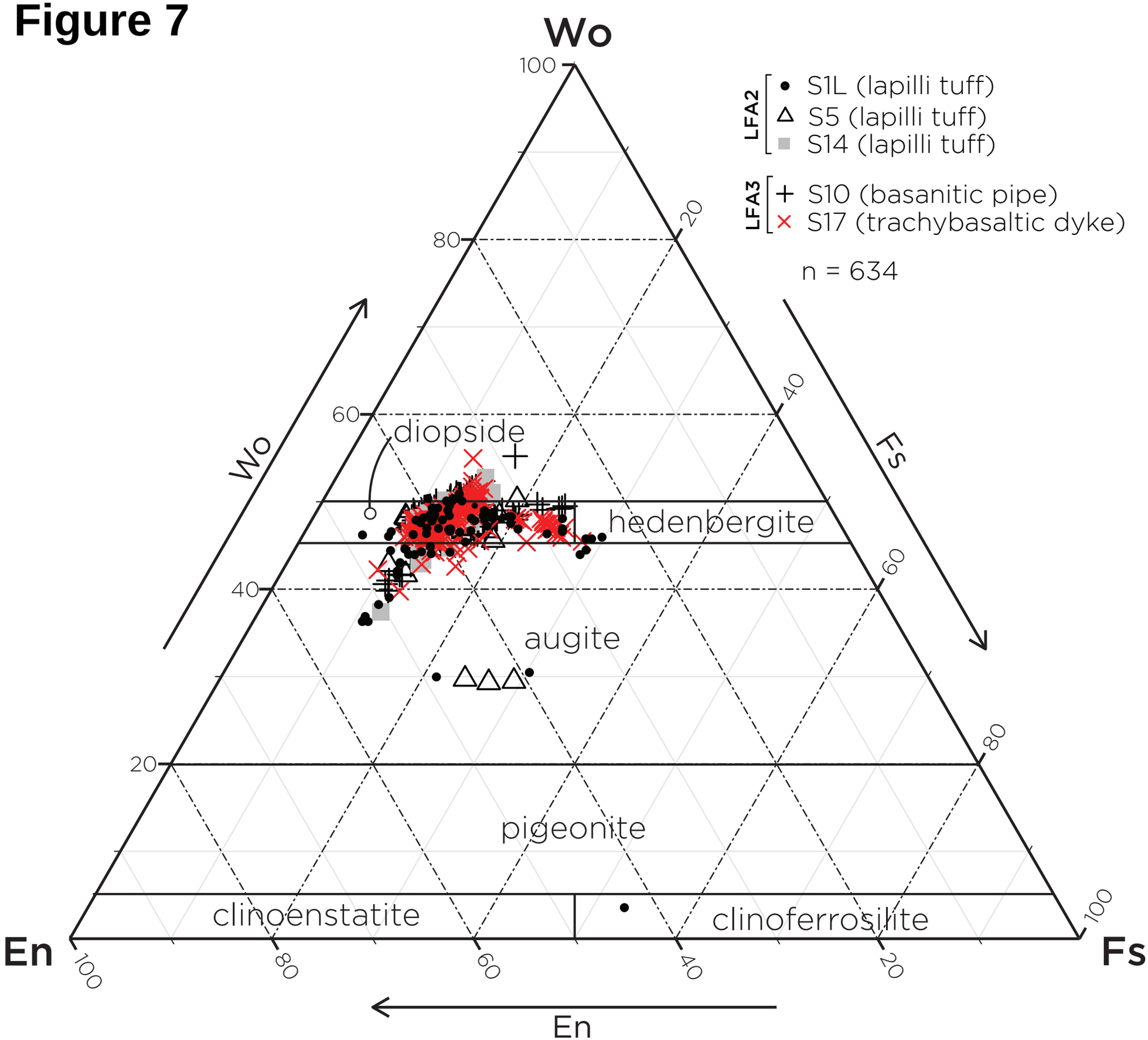
Wo
100
80
60
40
20
Wo
diopside
hedenbergite
augite
pigeonite
clinoenstatite
clinoferrosilite
Fs
En
En
Fs
LFA2
S1L (lapilli tuff)
S5 (lapilli tuff)
S14 (lapilli tuff)
LFA3
S10 (basanitic pipe)
S17 (trachybasaltic dyke)
n = 634

Figure 8

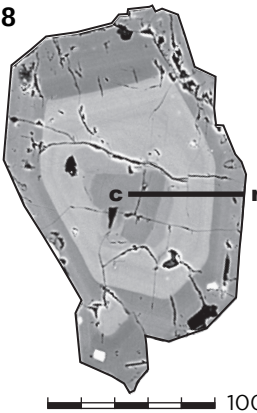
c
r


100 μm

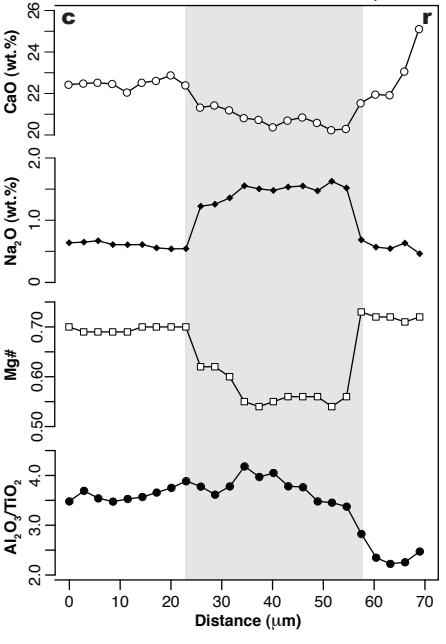
c
r
CaO (wt.%)
20
22
24
26
Na2O (wt.%)
0
1.0
2.0
Mg#
0.50
0.60
0.70
Al2O3/TiO2
2.0
3.0
4.0
0
10
20
30
40
50
60
70
Distance (μm)

Figure 9

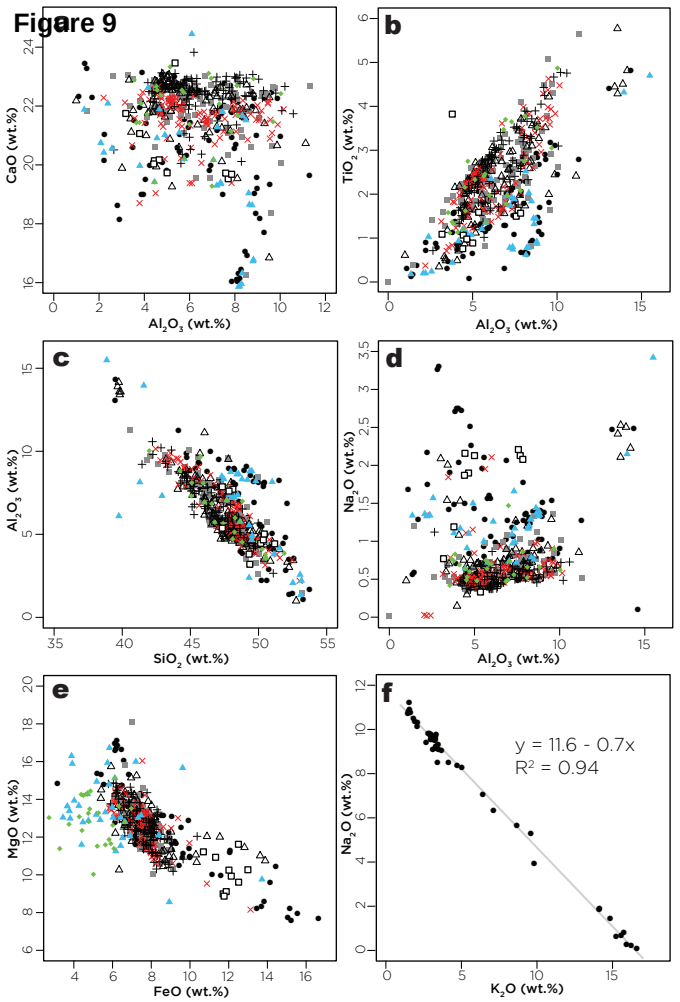

LFA2
- S1L (lapilli tuff)
- S14 (lapilli tuff)
- S5 (lapilli tuff)

LFA3
- S17 (basanite dyke)
- S10 (breccia pipe)

- Pyroxenitic cumulates
- Cpx. crystals
- Cpx. megacrysts & xenoliths (Wallis, 1989)

Figure 10

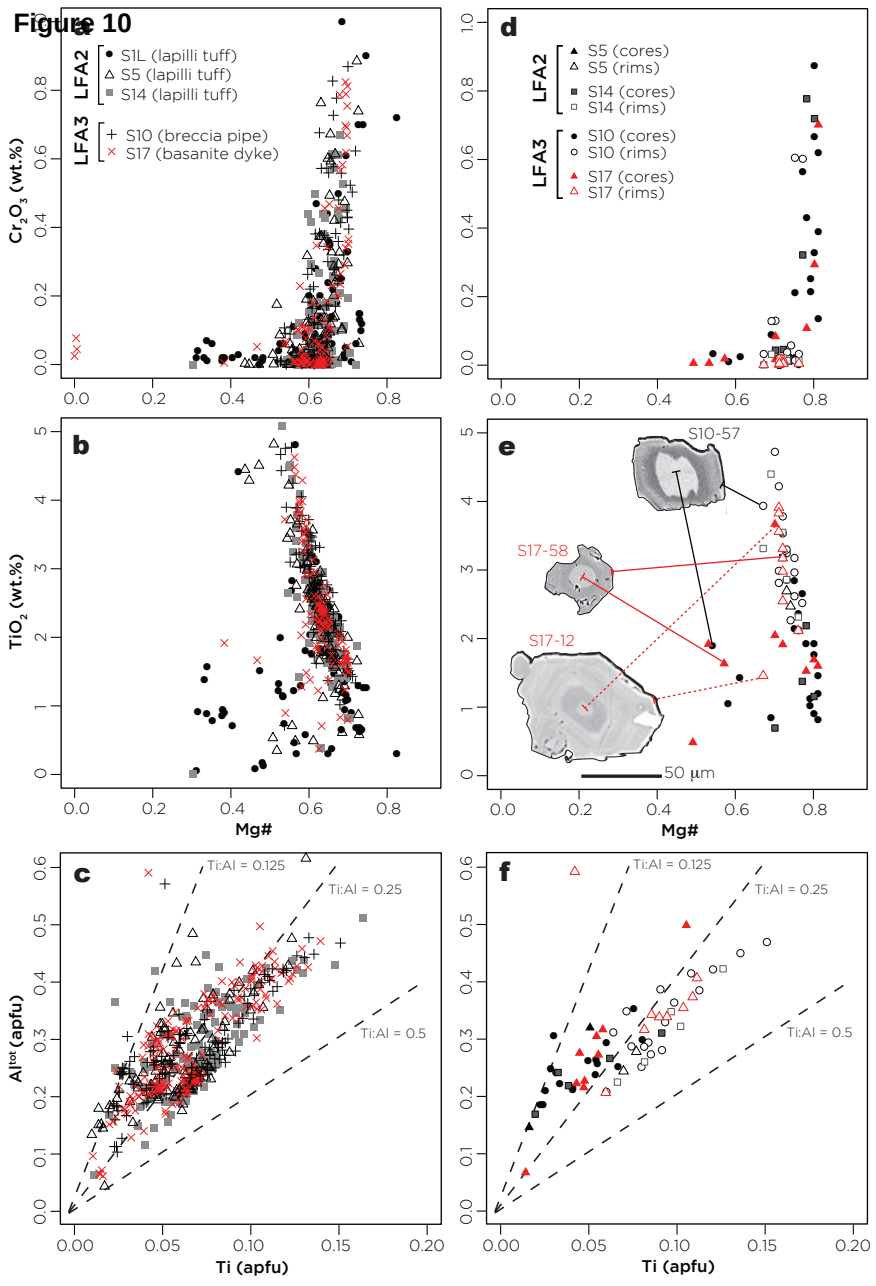
a
LFA2
S1L (lapilli tuff)
S5 (lapilli tuff)
S14 (lapilli tuff)
LFA3
S10 (breccia pipe)
S17 (basanite dyke)
Cr2O3 (wt.%)
d
LFA2
S5 (cores)
S5 (rims)
S14 (cores)
S14 (rims)
LFA3
S10 (cores)
S10 (rims)
S17 (cores)
S17 (rims)
b
TiO2 (wt.%)
Mg#
e
S10-57
S17-58
S17-12
50 µm
Mg#
c
Ti:Al = 0.125
Ti:Al = 0.25
Ti:Al = 0.5
Altot (apfu)
Ti (apfu)
f
Ti:Al = 0.125
Ti:Al = 0.25
Ti:Al = 0.5
Ti (apfu)

Figure 11

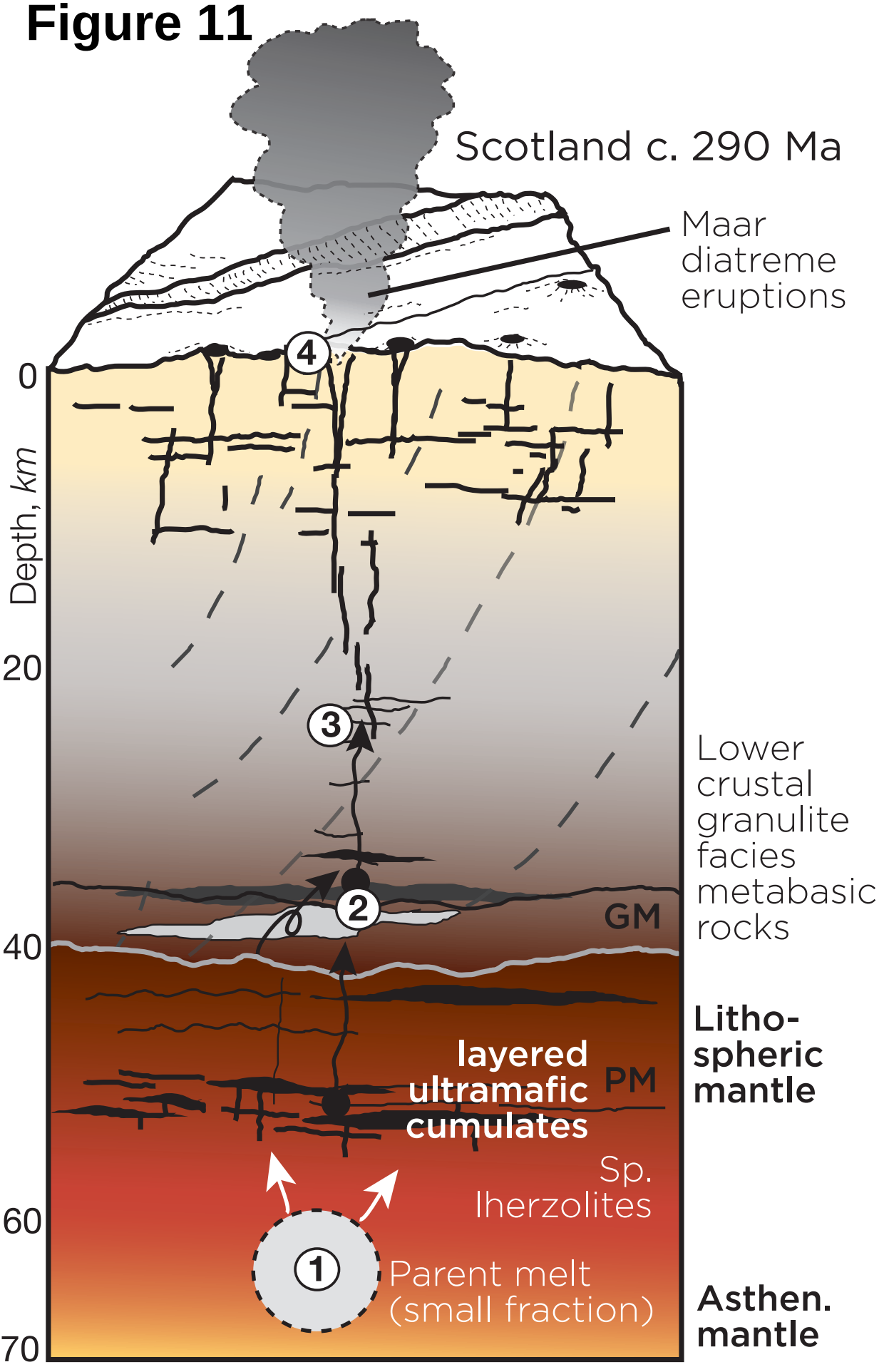
Scotland c. 290 Ma
Maar diatreme eruptions
4
0
Depth, km
20
3
Lower crustal granulite facies metabasic rocks
2
GM
40
Litho-spheric mantle
layered ultramafic cumulates
PM
Sp. lherzolites
60
1
Parent melt (small fraction)
Asthen. mantle
70

Figure 12

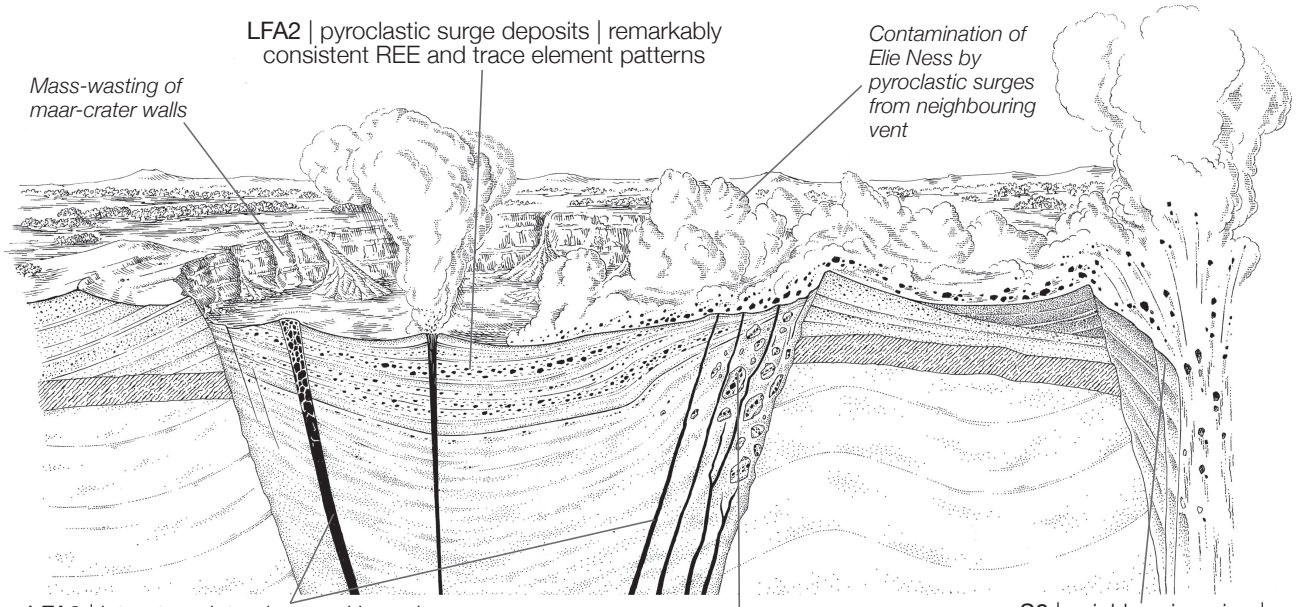
LFA2 | pyroclastic surge deposits | remarkably consistent REE and trace element patterns
Mass-wasting of maar-crater walls
Contamination of Elie Ness by pyroclastic surges from neighbouring vent
LFA3 | late-stage intrusives and breccia pipes | most geochemically diverse LFA (entrained mafic phases?)
LFA1 | vent-filling massive lapilli tuffs | considerable variation in REE and trace element patterns
S8 | neighbouring pipe | geochemically near-identical to LFA2